



HAL
open science

Present-Day and Historical Aerosol and Ozone Characteristics in CNRM CMIP6 Simulations

Martine Michou, P. Nabat, D. Saint-martin, J. Bock, Bertrand Decharme,
Marc Mallet, R. Roehrig, R. Séférian, S. Sénési, A. Voldoire

► **To cite this version:**

Martine Michou, P. Nabat, D. Saint-martin, J. Bock, Bertrand Decharme, et al.. Present-Day and Historical Aerosol and Ozone Characteristics in CNRM CMIP6 Simulations. *Journal of Advances in Modeling Earth Systems*, 2020, 12 (1), 10.1029/2019MS001816 . hal-03013972

HAL Id: hal-03013972

<https://hal.science/hal-03013972>

Submitted on 19 Nov 2020

HAL is a multi-disciplinary open access archive for the deposit and dissemination of scientific research documents, whether they are published or not. The documents may come from teaching and research institutions in France or abroad, or from public or private research centers.

L'archive ouverte pluridisciplinaire **HAL**, est destinée au dépôt et à la diffusion de documents scientifiques de niveau recherche, publiés ou non, émanant des établissements d'enseignement et de recherche français ou étrangers, des laboratoires publics ou privés.



RESEARCH ARTICLE

10.1029/2019MS001816

Special Section:

The CNRM Climate and Earth System Models for CMIP6

Present-Day and Historical Aerosol and Ozone Characteristics in CNRM CMIP6 Simulations

M. Michou¹, P. Nabat¹, D. Saint-Martin¹, J. Bock¹, B. Decharme¹, M. Mallet¹, R. Roehrig¹, R. S  ferian¹, S. S  n  si¹, and A. Voldoire¹¹CNRM, Universit   de Toulouse, M  t  o-France, CNRS, Toulouse, France

Key Points:

- The representations of aerosol and ozone in the CMIP6 CNRM-CM6-1 and CNRM-ESM2-1 models is described
- Present-day and historical aerosol and ozone distributions are assessed, as well as their effective radiative forcing (ERF)
- The present-day anthropogenic aerosol ERF (-1.10 W m^{-2} for CNRM-CM6-1) is sensitive to the interactivity of aerosols

Correspondence to:

M. Michou and P. Nabat,
martine.michou@meteo.fr;
pierre.nabat@meteo.fr

Citation:

Michou, M., Nabat, P., Saint-Martin, D., Bock, J., Decharme, B., Mallet, M., et al. (2020). Present-day and historical aerosol and ozone characteristics in CNRM CMIP6 simulations. *Journal of Advances in Modeling Earth Systems*, 12, e2019MS001816. <https://doi.org/10.1029/2019MS001816>

Received 16 JUL 2019

Accepted 11 DEC 2019

Accepted article online 17 DEC 2019

Abstract Characteristics and radiative forcing of the aerosol and ozone fields of two configurations of the Centre National de Recherches M  t  orologiques (CNRM) and Cerfacs climate model are analyzed over the historical period (1850–2014), using several Coupled Model Intercomparison Project 6 (CMIP6) simulations. CNRM-CM6-1 is the atmosphere-ocean general circulation model including prescribed aerosols and a linear stratospheric ozone scheme, while the Earth System Model CNRM-ESM2-1 has interactive tropospheric aerosols and chemistry of the midtroposphere aloft. The representations of aerosols and ozone in CNRM-CM6-1 are issued from simulations of CNRM-ESM2-1, and this ensures some comparability of both representations. In particular, present-day anthropogenic aerosol optical depths are similar (0.018), and their spatial patterns correspond to those of reference data sets such as MACv2 and MACv2-SP despite a negative bias. Effective radiative forcings (ERFs) have been estimated using 30-year fixed sea surface temperature simulations (piClim) and several calls to the radiative scheme. Present-day anthropogenic aerosol ERF, aerosol-radiation ERF, and aerosol cloud ERF are fully within CMIP5 estimates and, respectively, equal to -1.10 , -0.36 , and -0.81 W m^{-2} for CNRM-CM6-1 and -0.21 , -0.61 , and -0.74 W m^{-2} for CNRM-ESM2-1. Additional CMIP6-type piClim simulations show that these differences are mainly due to the interactivity of the aerosol scheme whose impact is confirmed when assessing the response of both climate model configurations to rising CO_2 . Present-day stratospheric ozone ERF, equal to -0.04 W m^{-2} , is in agreement with that of the CMIP6 ozone. No trend appears in the ozone ERF over the historical period although the evolution of the total column ozone is correctly simulated.

Plain Language Summary The manuscript documents the M  t  o-France Centre National de Recherches M  t  orologiques aerosol-chemistry modeling contributions to the sixth Coupled Model Intercomparison Project that supports the sixth IPCC Assessment Report of climate change. It establishes that their results are suitable for use by the scientific community in the analysis of the sixth Coupled Model Intercomparison Project experiments. The authors provide an evaluation of the model performance in both present-day and historical (1850–2014) contexts, as well as a detailed analysis of the model calculated effective radiative forcing due to ozone and aerosols.

1. Introduction

In the design of the Coupled Model Intercomparison Project 6 (CMIP6) presented in Eyring et al. (2016), several Model Intercomparison Projects (MIPs), including AerChemMIP (Aerosol Chemistry; see Collins et al., 2017) and RFMIP (Radiative Forcing; see Pincus et al., 2016), address the question of the quantification of the climate impacts of aerosols and various chemically reactive gases including ozone. Aerosols and ozone are part of the near-term climate forcers defined as those compounds whose impact on climate occurs primarily within the first decade of their presence in the atmosphere (Myhre, Shindell, et al., 2013). With regard to these two forcings, the variety of climate models involved in CMIP6 will range from models with both prescribed aerosols and ozone to models with fully interactive ozone chemistry and aerosol schemes. Therefore, official ozone and aerosol forcings have been developed (see <http://goo.gl/r8up31> and Stevens et al., 2017) and will be used by some of the CMIP6 models, notably in some specific CMIP6 simulations, for example, in RFMIP simulations (Pincus et al., 2016).

Forcing estimates of ozone and aerosols for the 1750–2011 period have been reported in the Fifth Assessment Report (AR5) of the International Panel on Climate Change (Myhre, Shindell, et al., 2013) with various confidence levels that range from high confidence with medium agreement for tropospheric and

  2019. The Authors.

This is an open access article under the terms of the Creative Commons Attribution License, which permits use, distribution and reproduction in any medium, provided the original work is properly cited.

stratospheric ozone and aerosol-radiation interactions to low confidence with low agreement for aerosol-cloud interactions. This uncertainty on the aerosol forcing is the main source of the uncertainty on the total anthropogenic forcing (Myhre, Shindell, et al., 2013).

Various forcing concepts have been used in the past to compare mechanisms that contribute to climate change. Quite recently, Myhre, Shindell, et al. (2013) have introduced the effective radiative forcing (ERF) concept that allows all physical variables to respond to perturbations except those concerning the ocean and sea ice. Characteristics of ERF calculations make ERF a better indicator of the surface temperature response of the climate system than the Radiative Forcing (RF) measure in which all surface and tropospheric conditions are kept fixed, even though internal variability of the climate model, mainly related to clouds, generates variability in ERF. ERF is then “the change in net top of the atmosphere (TOA) downward radiative flux after allowing for atmospheric temperatures, water vapor and clouds to adjust, but with global mean surface temperature or a portion of surface conditions unchanged” (Myhre, Shindell, et al., 2013). Two main methods are in use for these calculations: one with fixed sea surface temperatures (SSTs) and sea ice in a pair of simulations, a control simulation and a forcing agent perturbed simulation, and one regressing the TOA net downward radiation change against the surface temperature response from a pair of coupled ocean-atmosphere simulations (Gregory et al., 2004). The former technique appears more suitable for small forcings, the smaller the forcing the longer the simulations though, and is largely part of the RFMIP and AerChemMIP suite of coordinated experiments to detect both transient and present-day (PD) ERFs.

To address in particular the issues just described, the Centre National de Recherches Météorologiques (CNRM) climate model, developed by CNRM and Cerfacs, has been run in two configurations. The first one is a fully coupled atmosphere-ocean general circulation model, under the name CNRM-CM6-1 (Voldoire et al., 2019), while the second one is an Earth System Model one named CNRM-ESM2-1 Sférian et al. (2019). In addition to its physical-dynamical core constituted by CNRM-CM6-1, CNRM-ESM2-1 includes interactive aerosols, gaseous chemistry, land carbon feedbacks, and ocean biogeochemistry. For the CMIP6 simulations, both models share the same tuning choices (see a description of the tuning strategy in Voldoire et al., 2019) and have been run at the same horizontal and vertical resolutions, for instance, in the atmosphere at about 1.4 degrees around the equator over the horizontal and over 91 vertical levels (for additional details, see Sférian et al., 2019; Voldoire et al., 2019).

The CNRM-CM6-1 representation of aerosols and ozone is simpler than that of CNRM-ESM2-1, but the two representations are closely related as presented in details in this article. Indeed, for the aerosols, CNRM-CM6-1 considers evolving monthly tropospheric aerosol optical depth (AOD) fields of five types of tropospheric aerosols which have been generated using the interactive aerosol scheme of CNRM-ESM2-1. For ozone, the linear parameterization of CNRM-CM6-1 has monthly coefficients computed with simulations using the interactive chemistry scheme of CNRM-ESM2-1. Consistency is therefore ensured between the two models and this provides a framework to assess how Earth system processes can impact a climate model, in particular in its response to external forcings in climate projections (see Sférian et al., 2019).

The objectives of this paper are to document how CNRM CMIP6 climate models represent aerosols and ozone, and to assess the representation and ERFs of these components over the historical 1850–2014 period. This study will form a basis for future CMIP6 analyses, where associated processes are involved, and for the assessment of uncertainties, in particular in multimodel studies. Section 2 provides details on the CNRM-CM6-1 and CNRM-ESM2-1 modeling of aerosols and ozone. Section 3 analyzes how the present distributions of various aerosol optical properties and of ozone compare to those of reference data sets, with an emphasis on CMIP6 data sets, whereas section 4 focuses on their historical evolution. Finally, section 5 discusses the radiative forcings obtained in CNRM climate model simulations, both for the PD compared to the preindustrial (PI) period and over the entire historical period.

2. Methodology

2.1. Aerosol Representation in the CNRM Climate Models

2.1.1. The Interactive Aerosol Scheme TACTIC_v2

The aerosol scheme used in the CNRM climate models is referred to as TACTIC_v2 (Tropospheric Aerosols for ClimaTe In CNRM). It is an evolution of the modeling described in Michou et al. (2015) and Nabat et al. (2015), whose sensitivity to the representation of aerosols has been further evaluated in Watson et al. (2018). The aerosol scheme version was frozen before the final tuning phase of CNRM-CM6-1

(Voldoire et al., 2019) in order to generate the AOD fields needed to run the model. TACTIC_v2 simulates the physical evolution of five tropospheric aerosols that are supposed externally mixed: dust (DD; three size bins), primary sea salt (SS; three size bins), black carbon (BC; two bins separating hydrophilic and hydrophobic particles), organic matter (OM; two bins as for BC), and sulfate (SO₄; one bin). The representation of the sulfate aerosol involves several gaseous precursors, namely, SO₂, H₂S, and dimethylsulfide (DMS), which are gathered into a single gaseous variable.

Compared to the version used in Michou et al. (2015) and Nabat et al. (2015), the main new features of the aerosol scheme come from changes in the SS scheme. To correct for a systematic low bias of AOD over oceans, the SS emissions are now calculated according to the formulation of Grythe et al. (2014) (p. 1286, equation 7) that includes a dependence on SST given by Jaeglé et al. (2011). Tested against observed concentrations in Grythe et al. (2014), this formulation of sea-salt emissions has shown to give the best estimates of sea-salt concentrations compared to other formulations.

$$\frac{dF(D_p, U_{10}, SST)}{dD_p} = T_w(SST) \left[235 U_{10}^{3.5} \exp \left(-0.55 \left[\ln \left(\frac{D_p}{0.1} \right) \right]^2 \right) + 0.2 U_{10}^{3.5} \exp \left(-1.5 \left[\ln \left(\frac{D_p}{3} \right) \right]^2 \right) + 6.8 U_{10}^3 \exp \left(-1 \left[\ln \left(\frac{D_p}{30} \right) \right]^2 \right) \right], \quad (1)$$

where $\frac{dF}{dD_p}$ is the source function in terms of number of aerosols by particle size by area by time, D_p the dry diameter, and U_{10} the wind speed at 10 m. The dependence to SST is

$$T_w(SST) = 0.3 + 0.1 SST - 0.0076 SST^2 + 0.00021 SST^3. \quad (2)$$

The dust emission module relies on the studies of Marticorena and Bergametti (1995) and Kok (2011), as described in Nabat et al. (2015). Dust particles are emitted in function of surface wind and land surface characteristics. The latter characteristics include soil textures, surface roughness length, and superficial soil moisture and are given by the land surface module embedded in the SURFEX surface modeling platform, detailed in Decharme et al. (2019).

With regard to anthropogenic and biomass burning emissions, TACTIC_v2 considers the static monthly mean 1750–2014 emissions inventories of BC, OM, and SO₂ recommended for the CMIP6 simulations. Anthropogenic sources (horizontal resolution of 0.5 degrees) are described in Hoesly et al. (2018) and biomass burning sources (0.25 degrees) in van Marle et al. (2017). Hoesly et al. (2018) indicate that their inventories, which benefited from improved methodologies and source information, are in general slightly higher than previous inventories. van Marle et al. (2017) analyze that global biomass emissions, with 1997–2015 GFED4s data as an anchor point, have been relatively constant over the entire 1750–2014 period, with regions of higher emissions due to deforestation and regions of lower emissions linked to changes in agricultural practices. All these inventories have been interpolated with a bilinear method to the CNRM grid at 1.4 degrees resolution. It is worth mentioning that, as in Michou et al. (2015), a multiplier coefficient of 1.5 has been applied to organic carbon emissions in order to take into account the conversion of organic carbon into organic matter. Such a conversion factor is a common practice and was originally based on analysis of fresh urban emissions (Turpin & Lim, 2001). In particular, this ratio ranges from 1.5 to 1.8 in the case of fresh particles emissions from biomass burning (Ng et al., 2010; Tiitta et al., 2014). Secondary organic aerosols (SOA) are taken into account through a monthly inventory given by Dentener et al. (2006), and DMS emissions follow the data set of Kettle et al. (1999). In addition, in order to avoid unrealistic large AOD peaks, emissions have been leveled off: SO₂ and BC emissions are limited to $5 \cdot 10^{-10} \text{ kg} \cdot \text{m}^{-2} \cdot \text{s}^{-1}$, while OM emissions are limited to $3 \cdot 10^{-9} \text{ kg} \cdot \text{m}^{-2} \cdot \text{s}^{-1}$. A threshold of $5 \cdot 10^{-10} \text{ kg} \cdot \text{m}^{-2} \cdot \text{s}^{-1}$ is applied to SO₂ emissions coming from gaseous volcanic emissions (Andres & Kasgnoc, 1998). All emissions are injected into the lowest model level, and AODs are those of the grid-box mean conditions.

The TACTIC_v2 interactive aerosol scheme is used in all CMIP6 simulations carried out with CNRM-ESM2-1.

Table 1

Aerosol Optical Properties by Species at 550 nm and 80% Relative Humidity for TACTIC_v2, MACv2, and the MERRA-2 Reanalysis

Species	Single scattering albedo			Asymmetry parameter		
	TACTIC_v2	MACv2	MERRA-2	TACTIC_v2	MACv2	MERRA-2
SO ₄	0.997	1.00	1.00	0.74	0.67–0.70	0.78
OM	0.997	0.97	0.97–0.98	0.74	0.56–0.62	0.58–0.68
SS	0.996	0.999	1.00	0.78	0.75	0.50–0.86
DD	0.90	0.86–0.96	0.77–0.96	0.785	0.73–0.83	0.71–0.87
BC	0.32	0.21–0.27	0.21–0.25	0.43	0.27–0.33	0.33–0.40
Stratospheric	0.999	NA	NA	0.73	NA	NA

Note. MACv2 and MERRA-2 values represent the range for a given species.

2.1.2. The Aerosol Data Set for CNRM-CM6-1

In the standard GCM configuration of CNRM-CM6-1, this interactive aerosol scheme is not activated and is replaced by monthly AOD fields of BC, OM, SO₄, DD, and SS varying each year. As described in Voldoire et al. (2019), these AOD fields have been calculated in preliminary CNRM-CM6-1 AMIP-type (atmosphere only) historical and future simulations using the interactive aerosol scheme described above and observed SSTs and sea ice (CMIP6 data). This historical simulation is named amip-hist-aod in the present study (see Table 2). Its AOD outputs for each aerosol type have been smoothed out using an 11-year running mean. The resulting AOD data set is used as the source of aerosol forcing in all CNRM-CM6-1 CMIP6 simulations.

2.1.3. The Aerosol-Radiation-Cloud Interactions

CNRM-CM6-1 and CNRM-ESM2-1 use the same parameterizations for representing interactions between aerosols, clouds, and radiation. The radiative transfer scheme receives 3-D distributions of aerosol extinction, either directly calculated by the interactive aerosol scheme in CNRM-ESM2-1 or coming from the vertical distribution of AODs in CNRM-CM6-1. This vertical distribution in CNRM-CM6-1 depends only on the aerosol type and is therefore unchanged in time and space. It is calculated from a pressure-dependent function using a scale height specific to each aerosol type as described in Bozzo et al. (2019). Other aerosol optical properties used as input in the radiative transfer scheme, both in CNRM-CM6-1 and CNRM-ESM2-1, namely, the single scattering albedo (SSA; 0 to 1 range) and the asymmetry parameter (ASY; –1 to 1 range), are prescribed depending on the aerosol type, relative humidity (except for DD and BC), and wavelength. All our aerosol properties have been calculated with the Mie theory using refractive indexes of Krekov (1993) for each aerosol type and have been published in Table 6 of Nabat et al. (2013). For the sake of brevity, Table 1 only shows values at 550 nm and 80% relative humidity, together with MACv2 values, based in part on AERONET observations, and MERRA-2 Aerosol Reanalysis values. MACv2 (Kinne, 2019) and MERRA-2 (see Randles et al., 2017, supplementary material) describe their choices of refractive indices and/or aerosol size distributions which lead to their aerosol optical properties. Differences in these properties highlight uncertainties on these parameters, especially for BC.

With regard to aerosol-cloud interactions, CNRM-CM6-1 and CNRM-ESM2-1 only represent the first aerosol indirect (or Twomey) effect whereby aerosols increase the number of cloud droplets at constant liquid water content thus reducing cloud droplet size and increasing cloud albedo. No secondary aerosol indirect effects (impact of particles on precipitation) are included in either models. The Twomey effect is parameterized through the calculation of cloud droplet number concentration (CDNC; cm^{–3}) which is related to changes in aerosol concentrations (μg m^{–3}). The parameterization of Menon et al. (2002) has been chosen in order to take into account the Twomey effect caused by SO₄, OM (hydrophilic part), and SS (first size bin), as it had been done in the ECMWF IFS model (Michou et al., 2015; Morcrette et al., 2011). Note that the effects of DD and BC are not taken into account in this formulation that reads

$$CDNC = 10^{[b+a_{SO_4} \log_{10}(m_{SO_4})+a_{SS} \log_{10}(m_{SS})+a_{OM} \log_{10}(m_{OM})]} \quad (3)$$

Several values of the associated coefficients have been tested based on the uncertainty ranges given in several studies (Boucher & Lohmann, 1995; Menon et al., 2002; Quaas & Boucher, 2005; Quaas et al., 2006). In particular, we varied a_{SO_4} from 0.2 to 0.5 and b from 1.7 to 2.41. These sensitivity tests resulted in estimates of the ERF due to aerosol-cloud interactions of the anthropogenic aerosols ranging from –1.9 to 0.1 W m^{–2} (the

methodology to calculate this ERF is presented in section 5.1). Additional details on the sensitivity of the CNRM climate models to these parameters are provided in Watson et al. (2018). The final set of coefficients, $a_{SS} = 0.05$, $a_{OM} = 0.13$, $a_{SO_4} = 0.20$ and $b = 2.20$, has been chosen to best fulfill some of the metrics described in Quaas et al. (2009).

2.2. The Ozone Representation in the CNRM Climate Models

2.2.1. The Chemistry Scheme in CNRM-ESM2-1

The chemistry scheme of CNRM-ESM2-1, identified in CMIP6 simulations under the name REPROBUS-C_v2, was implemented in the CNRM climate model and evaluated in Michou et al. (2011). This climate model version also contributed to the Chemistry Climate Model Initiative (e.g., Maycock, Matthes, et al., 2018; Maycock, Randel, et al., 2018; Morgenstern et al., 2017; Wales et al., 2018; Zhang et al., 2018). It is an “online” scheme whereby the chemistry routines are part of the physics of the atmospheric climate model and called at each time step of the physics. The scheme does not represent the low troposphere ozone nonmethane hydrocarbon chemistry. It considers 168 chemical reactions, among which 39 are photolysis ones and 9 represent the heterogeneous chemistry. Chemical evolution is computed down to 560 hPa (for details, see Michou et al., 2011, and Morgenstern et al., 2017). Below this level, concentrations of a number of species (i.e., N_2O , CH_4 , CO , CO_2 , CFC11, CFC12, CFC113, CCl_4 , CH_3CCl_3 , CH_3Cl , HCFC22, CH_3Br , H1211, and H1301) are relaxed toward the yearly evolving global mean abundances of CMIP6 (Meinshausen et al., 2017); for the remaining species, concentrations below 560 hPa are relaxed toward the 560 hPa value. Consistently with the relaxation, explicit emissions, dry deposition, washout, and parameterized transport (diffusion and convection) of the chemical fields are not considered. The 3-D concentrations of a number of trace gases interact with the atmospheric radiative code at each call of the radiative scheme (every 1 hr), for the longwave (LW) part of the spectrum (H_2O , CO_2 , O_3 , CH_4 , N_2O , CFC11, and CFC12) and for its shortwave (SW) counterpart (O_3 , H_2O , and CO_2). Running the REPROBUS-C_v2 chemistry scheme adds about 50% computing time.

Overall, differences between the current and the Michou et al. (2011) versions of the chemistry have been motivated by taking into account existing updates (e.g., new kinetics) and evolutions of the climate model, in particular evolution with regard to its vertical extension that required small adjustments both at the top and at the bottom of the atmosphere to simulate satisfactory concentrations of chemical species and evolution toward an Earth system model that considers the full carbon cycle. These differences consist in

- Kinetics and photolysis rates are now those of Sander et al. (2011).
- Monthly distributions of stratospheric sulfate aerosols follow the CMIP6 recommendations: Concentration, surface area density, and volume density are based on the work of Thomason et al. (2018).
- Solar information also follows the CMIP6 recommendations (Matthes et al., 2017). The CNRM climate model uses monthly averages to modulate photolysis rates.
- Photolysis rates are no longer modified according to cloudiness as we could not see any impact of this correction factor on the diagnostics of the upper troposphere and of the stratosphere covered by our chemistry scheme and as the correction factor was developed for a CTM aimed at studying tropospheric ozone and its precursors (Brasseur et al., 1998).
- A different processing between the surface and the 560 hPa level as detailed above.
- The chemistry scheme vertical extension has been updated following that of the climate model, which now covers the atmospheric layer going from the surface to about 80 km in the mesosphere with 91 vertical levels. This did not require any specific adjustment except for the relaxation of H_2O performed toward 6.5 ppmv over the seven highest model levels (above 0.5 hPa).
- The chemistry variables increased to 63, with 44 fields transported by the CNRM-ESM2-1 dynamical core. The remaining chemical fields are supposed in chemical equilibrium.
- The scheme has been extended to consider CO_2 emissions (anthropogenic and natural sources) and transport, so that CNRM-ESM2-1 can be driven by CO_2 emissions and thus contribute to the associated CMIP6 experiments.

2.2.2. The Ozone Linear Scheme in CNRM-CM6-1

The ozone chemistry scheme used in CNRM-CM6-1 is a modified version of the one used in CNRM-CM5.1 (VolDOIRE et al., 2013). Eyring et al. (2013) emphasized the main weaknesses of the CNRM-CM5.1 version, in particular a large underestimation of past ozone depletion. Therefore, the authors had excluded CNRM-CM5.1 from the multimodel analysis of the future evolution of ozone. The simplicity and low computational cost of this scheme was retained for CNRM-CM6-1. The scheme is a linearized version of the

Table 2
List of Simulations Used in the Present Study, Along With Their Characteristics

Name	Model	CMIP6	Members	Oce/atm	Figures	Tables
amip-hist-aod	CNRM-CM6-1+TACTIC_v2	n	1	No	2, 3, and 9	4 and 5
historical	CNRM-CM6-1	y	6	Yes	1, 4, 5, 8, and 10	
historical	CNRM-ESM2-1	y	5	Yes	4, 5, 8, and 10	
amip-hist	CNRM-CM6-1	y	10	No	10	
amip-hist	CNRM-ESM2-1	y	1	No	10	
ERF simulations (see Tables 7, 8 and 9)					11, 12, 13, and 14	10 and 11

Note. Oce/Atm indicates ocean-atmosphere coupled simulations.

REPROBUS-C_v2 ozone component and describes the ozone net production as a linear function of the ozone mixing ratio (r_{O_3}), the temperature T , and the ozone column above the grid point Σ_{O_3} . In CNRM-CM5.1, a fourth variable was used, namely, the equivalent chlorine content of the stratosphere, to account for ozone heterogeneous chemistry. This term proved to be problematic in CNRM-CM5.1 and resulted in an inaccurate treatment of heterogeneous ozone chemistry, as in other models (Monge-Sanz et al., 2011). Therefore, after unfruitful attempts to retain this term, we chose to keep only the first three variables of the linear scheme, as in Monge-Sanz et al. (2011), and we embedded in the set of new A_i coefficients the heterogeneous chemistry scheme. Evolution of the ozone mixing ratio r_{O_3} in CNRM-CM6-1 now reads

$$\frac{\partial r_{O_3}}{\partial t} = A_1 + A_2(r_{O_3} - A_3) + A_4(T - A_5) + A_6(\Sigma_{O_3} - A_7), \quad (4)$$

with $A_1 = P - L$ where P and L are the respective ozone production and loss, $A_2 = \partial(P - L)/\partial r_{O_3}$, $A_3 = \bar{r}_{O_3}$ the monthly average of r_{O_3} , $A_4 = \partial(P - L)/\partial T$, $A_5 = \bar{T}$ (temperature), $A_6 = \partial(P - L)/\partial \Sigma_{O_3}$, and $A_7 = \bar{\Sigma}_{O_3}$.

All A_i coefficients are monthly evolving values computed in the course of AMIP simulations with the CNRM climate model in which the REPROBUS-C_v2 scheme was activated. For the CMIP6 historical period, an ensemble of three AMIP simulations with CMIP6 forcings have been performed over 1950–2014, considering that A_i coefficients could be set to 1950 ones prior to 1950. By construction, the CNRM-CM6-1 ozone concentrations should closely follow those of CNRM-ESM2-1. A similar strategy based on AMIP simulations has been set up for the scenarios.

2.3. Experimental Settings

All the simulations used here are presented in Table 2. They cover the 1850–2014 historical period (165 years). The number of members is also noted in Table 2, as well as the figures and tables of this article where they are used. By construction, there is no difference in the aerosol loadings of the various members of an ensemble of CNRM-CM6-1 simulations. Additional diagnostics come from the amip-hist-aod simulation, performed to produce the AOD used in CNRM-CM6-1. Most simulations concern the CNRM-CM6-1 model, but a few simulations with CNRM-ESM2-1 are also analyzed to highlight specific similarities or differences between the two models.

2.4. Reference Data Sets

Our assessment is fully placed in the CMIP6 context, with the objective to provide information to relate our results with those obtained with other models using “official” CMIP6 prescribed ozone and/or aerosol fields (see CMIP6 input4MIPs page, <https://esgf-node.llnl.gov/projects/input4mips/>). So our initial reference data sets are these official CMIP6 data sets, and then we enlarged slightly our analysis to closely related data sets.

More specifically, two aerosol data sets are used as references. The first one provides aerosol optical properties and an estimate of the Twomey effect computed with an off-line version of the MACv2-SP (Simple Plume) code Stevens et al. (2017), run on a T63 grid (courtesy of S. Fiedler). It is thereafter referred to as the MACv2-SP aerosol data set. The Simple Plume code has been developed to be implemented in climate models to investigate some of the aerosol effects on the climate system (e.g., within RFMIP; see Pincus et al., 2016). It has already been used in several publications (Fiedler et al., 2017, 2019; Nordling et al., 2019).

The second aerosol data set used in this paper is the 2017 version of the Max Planck Institute Aerosol Climatology (MACv2; Kinne, 2019), which is an update of the MAC-v1 climatology described in Kinne et al. (2013)

Table 3

Emission Totals (Means $\pm\sigma$), for the Beginning (1850–1859) and the End (2005–2014) of the CMIP6 Historical Period, as well as Present-Day Estimates From the Literature

Species	Source	amip-hist-aod		Literature
		1850–1859	2005–2014	present day
BC	Total	2.50 \pm 0.05	8.77 \pm 0.33	12 \pm 3 ^a , 15 \pm 14 ^b
	BB	1.61 \pm 0.03	1.75 \pm 0.17	
OM	Total	58.97 \pm 0.51	78.86 \pm 2.26	97 \pm 25 ^a , 119 \pm 111 ^b
	BB	20.12 \pm 0.41	18.07 \pm 1.39	
	SOA	32.16 ^e	32.16 ^e	19 (13–121) ^c
All SO ₄ prec.	Total	45.67 \pm 0.33	134.99 \pm 4.65	119 \pm 26 ^a
SO ₂	BB	2.02 \pm 0.04	2.15 \pm 0.15	
	Volcanoes	2.93	2.93	29.2 ^e
DMS	Total	39.78 ^h	39.78 ^h	20–80 ^d
SO ₄	Total	3.27 \pm 0.02	9.96 \pm 0.35	
DD	Total	3,485.48 \pm 82.04	3,537.16 \pm 100.45	1,123 (514;4,313) ^f
SS	Total	288.4 \pm 4.1	299.7 \pm 5.8	1.8 to 2,444 ^g

Note. BB refers to biomass burning emissions. BC, OM, SOA, and DD emissions are in Tg year⁻¹, all sulfur species in Tg(SO₂) year⁻¹, and SS in Pg year⁻¹.

^aAeroCom mean $\pm\sigma$ (intermodel) (Textor et al., 2006, Table 10). ^bMean $\pm\sigma$ (intermodel) (Huneus et al., 2012, Table 5). ^cTsigaridis et al. (2014) mean and range from models. ^dBoucher et al. (2013) (Table 7.1 range). ^eDentener et al. (2006). ^fHuneus et al. (2012) (AeroCom median and range). ^gGrythe et al. (2014) range. ^hKettle et al. (1999).

and used in a number of climate studies (Michou et al., 2015; Toll et al., 2016) and which is the baseline MACv2-SP attempts to approximate. This data set provides monthly aerosol optical properties on a 1 degree grid, derived from a combination of observations and model outputs. Observations include the AERONET ground-based sun photometers network (Holben et al., 1998; <http://aeronet.gsfc.nasa.gov>), as well as measurements over ocean provided by the Maritime Aerosol Network (Smirnov et al., 2009). Model outputs are derived from the AeroCom global modeling initiative (e.g., Kinne et al., 2006; Koffi et al., 2016; <https://aerocom.met.no/references.html>, for the list of AeroCom related references). MACv2 covers the 1850–2100 period and includes interannual variability for the anthropogenic aerosols, while natural aerosols consider only monthly variations. Optical properties for the main aerosol types (i.e., DD,SS, BC, OM, and SO₄) are provided.

One could argue that as MACv2-SP is a fit to MACv2, there is not much to learn by comparing to MACv2-SP in addition to comparing to MACv2. However, as MACv2-SP is an official CMIP6 forcing, the comparison of CNRM results against this data set is a basic pillar of the present study. Second, MACv2 appears as a rather obvious data set to enlarge to other aerosol properties an analysis using MACv2-SP which describes only anthropogenic aerosol properties. Lastly, the evaluation of our model outputs in terms of aerosols against observations from the real world is not presented here as it had already been done in a previous version of TACTIC (Michou et al., 2015) and then in several other papers following the evolution of the scheme (Drugé et al., 2019; Nabat et al., 2015; Watson et al., 2018), as well as “in-house,” all along model developments.

With regard to ozone, the official CMIP6 ozone forcing (see <http://goo.gl/r8up31>) is referred to, in this paper, as CMIP6-OZ. CMIP6-OZ provides monthly 3-D ozone mixing ratios from 1850 to 2014 on a 96 \times 44 lat-lon grid and on 66 pressure levels from 1,000 to 0.0001 hPa. The tropospheric and stratospheric ozone forcings computed with CMIP6-OZ are analyzed in Checa-Garcia et al. (2018).

Finally, we considered NIWA3.3 ozone data from the National Institute of Water and Atmospheric Research (NIWA) Bodeker Scientific research (<http://www.bodekerscientific.com/home>) which has a history of developing ozone data sets for climate research. NIWA3.3 data are the so-called “combined patched” monthly data that extend from November 1978 to December 2016 and combine satellite-based ozone measurements from various instruments, including more recently those of the NPP-OMPS and SCIAMACHY ones and including also measurement uncertainty estimates. Patches as spatial linear interpolations fill in data gaps (see <http://www.bodekerscientific.com/data/total-column-ozone>, and Struthers et al., 2009).

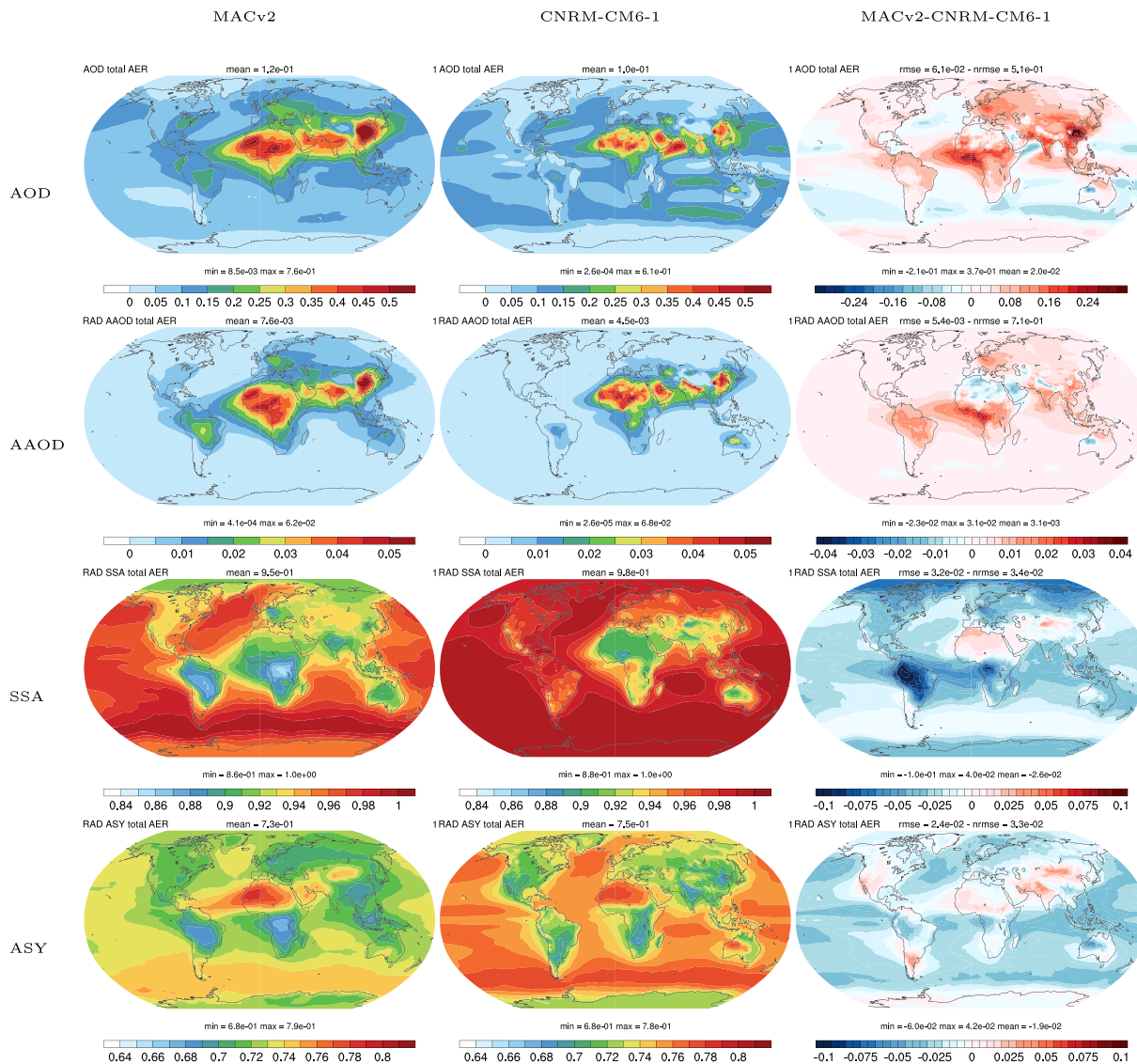


Figure 1. Mean optical properties (550 nm) of total aerosols around 2005. From left to right MAC-v2, CNRM-CM6-1, and difference MAC-v2-CNRM-CM6-1. And from first line to last line annual means of AOD, AAOD, SSA, and ASY.

3. Evaluation of PD Characteristics of Aerosols and Ozone

3.1. Aerosol Optical Properties

Characteristics of aerosol loads and distributions are determined to a large extent by characteristics of their respective emissions. Table 3 presents 10 year means of the total yearly emissions over the globe for the various aerosols in the amip-hist-aod simulation, for the beginning and the end of the 1850–2014 period, together with other total emissions reported in the literature for PD emissions, derived from observations or from various modeling exercises. The TACTIC_v2 emission budget agrees well with current estimates that can be found in the literature or at least falls within the large uncertainty ranges reported in Table 3. The only notable exceptions concern SS and volcanic SO₂ emissions. We identified two main causes for this overestimation of SS emissions (as well as boundary layer SS mixing ratios, not shown): First, SS masses are expressed at 80% humidity, unlike the other aerosol masses which are expressed as dry masses, and thus include hygroscopic growth and change in density. Second, the largest SS particles with a bin of 20 μm (radius at 80% humidity) are quite large compared to other models often limited to 10 μm. However, ultimately, optical properties of SS aerosols are in the range of observations.

Table 4

Global Mean Values Around 2005 of the Aerosol Optical Properties Presented in Figures 1–3, and Associated NRMSE for MACv2-SP and CNRM-CM6-1

Parameter	MACv2	MACv2-SP	CNRM-CM6-1	MACv2-SP	CNRM-CM6-1
	mean	mean	mean	NRMSE	NRMSE
Total AOD	0.12		0.10		0.51
Total AAOD	0.0076		0.0045		0.72
SSA	0.95		0.98		0.034
ASY	0.73		0.75		0.035
Ant. AOD	0.030	0.023	0.018	0.63	0.87
Ant. AAOD	0.0027	0.0018	0.0017	0.79	0.95
Nat. AOD	0.090		0.083		0.53
Nat. AAOD	0.0021		0.0027		1.4

Figure 1 shows the mean 2000–2009 optical properties of the MACv2 and CNRM-CM6-1 historical sets, namely, the AOD, Aerosol Absorption Optical Depth ($AAOD = (1 - SSA) \times AOD$), SSA, and ASY parameters at 550 nm for all aerosols, and Table 4 presents the global mean values for these different parameters and the normalized spatial root mean square error (NRMSE) defined as the ratio between the root mean square error (rmse) and the global mean of the reference data set (MACv2). The 2000–2009 period is centered on Year 2005 which is the anchor year of MACv2. The AOD is larger for MACv2 (0.12 global mean) than for CNRM-CM6-1 (0.10). Flato et al. (2013) and more recently Sockol and Small Griswold (2017) allow to put this difference into perspective. Flato et al. (2013) indicate that CMIP5 models (21) underestimate the mean observed 2001–2005 AOD by at least 20% over most land surfaces, and Sockol and Small Griswold (2017) report that the five CMIP5 models they have considered specifically in their study have mean AOD differences with MODIS observations (2000–2005) ranging from 0.01 (overestimation) to -0.09 . The largest biases in CNRM models occur over the Gulf of Guinea and the Equatorial Atlantic, with larger exports of dust and biomass burning aerosols for MACv2, over Asia including China and India, and to a lesser extent, over Europe. Over Central Africa and Amazonia, CNRM-CM6-1 bias could be reduced by scaling up biomass burning emissions, as commonly done in other models (Johnson et al., 2016); not scaling the official CMIP6 emissions appeared to us as preferable to better assess the intrinsic performance of our aerosol model. Over China and Europe, the negative bias could be due, for a part, to the absence of nitrate aerosols in TACTIC_v2. Indeed, such aerosols can cause an additional AOD of about 0.1 over China (Bellouin et al., 2011) and of about 0.08–0.1 over Europe (Drugé et al., 2019). Over South Asia, the AOD negative bias is an identified issue detected in different GCMs (Pan et al., 2015). Their mean annual biases range from 15% to 44% compared to MISR.

Figures 2 and 3 emphasize the anthropogenic and natural contributions to the AOD. The MACv2 and MACv2-SP data sets suppose that 1850 conditions are the reference conditions for anthropogenic aerosols. For a fair comparison, anthropogenic optical properties for the CNRM models are computed using the same hypothesis: For instance, anthropogenic AOD of a given year is the anomaly of the ($SO_4 + BC + OM$) AOD relative to 1850, noting that TACTIC_v2 assumes that DD is completely natural, and natural AOD includes the residual ($SO_4 + BC + OM$) AOD in addition to SS and DD AOD. Over India, differences are due to differences in natural aerosols, possibly exports of dust from the Arabian peninsula, while over China, they are essentially linked to anthropogenic sources. Overall, the NRMSE of CNRM-CM6-1 is larger for the anthropogenic aerosols than for the natural or total aerosols (0.87, 0.53, and 0.51, respectively). Furthermore, one can note that anthropogenic AOD differences between MACv2 and MACv2-SP are also large over China, while the two data sets are within 0.05 over the rest of the globe, highlighting the difficulty in representing aerosols over China. The PD proportion of anthropogenic AOD over total AOD is 25% for MACv2, against 18% for CNRM-CM6-1. Both proportions are within the range of the AeroCom Phase II models, estimated at $24\% \pm 0.06$ (Myhre, Samset, et al., 2013), although these figures hide much larger regional differences. The latter potentially impacts the aerosol radiative forcing, as argued in Carslaw et al. (2013) who demonstrated that uncertainties in natural aerosols are the major contributor to the uncertainty of the aerosol indirect forcing. Description and analysis of radiative forcing appear in section 5.1.

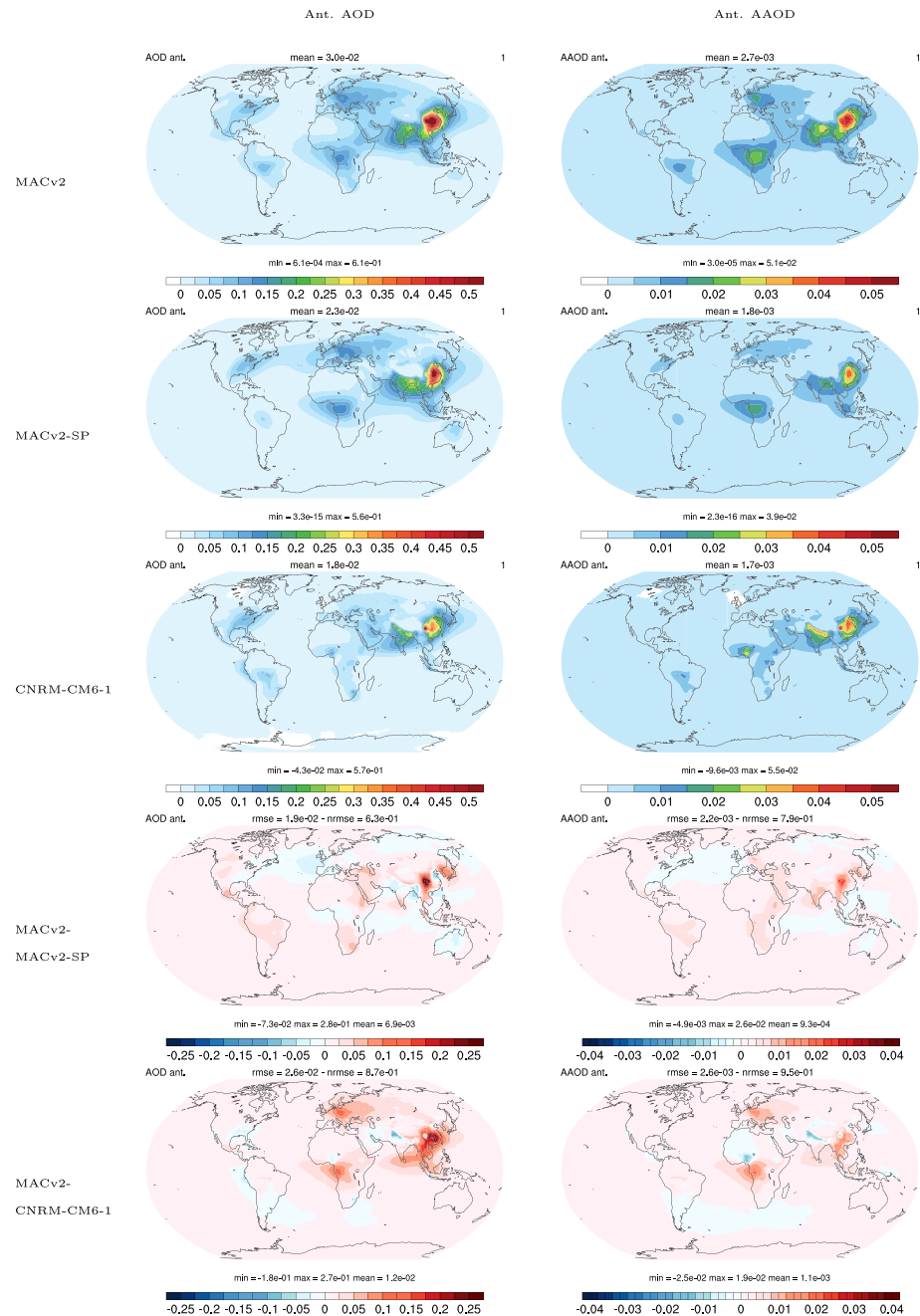


Figure 2. Mean annual AOD and AAOD around 2005 of anthropogenic aerosols. From first to last lines MACv2, MACv2-SP, CNRM-CM6-1, difference MACv2-MACv2-SP, and difference MACv2-CNRM-CM6-1. Means of 2000–2009 for CNRM-CM6-1 and MACv2 Ant. AOD, 2005 for the other MACv2 fields, and 2000–2005 for MACv2-SP.

Table 5 presents additional statistics for the AOD and AAOD, namely, their means calculated separately over land and ocean for CNRM-CM6-1, MACv2, the MERRA-2 aerosol reanalysis (Randles et al., 2017), and the CAMS reanalysis project (Inness et al., 2019). It confirms the too low CNRM-CM6-1 AOD, and it indicates that most of the global bias in AOD comes from a bias over land.

AAOD, which has been shown to be the biggest contributor to the aerosol direct effect uncertainty (see Lacagnina et al., 2015, and references therein), is larger in MACv2 than in CNRM-CM6-1 over all the equatorial continents (see Figures 2 and 3). This is related to the differences in SSA, whose global mean is smaller in MACv2 (0.95) than in CNRM-CM6-1 (0.98). Note that this CNRM-CM6-1 value is slightly outside the range of the AeroCom models (0.95 ± 0.02 ; Myhre, Samset, et al., 2013). Differences are the

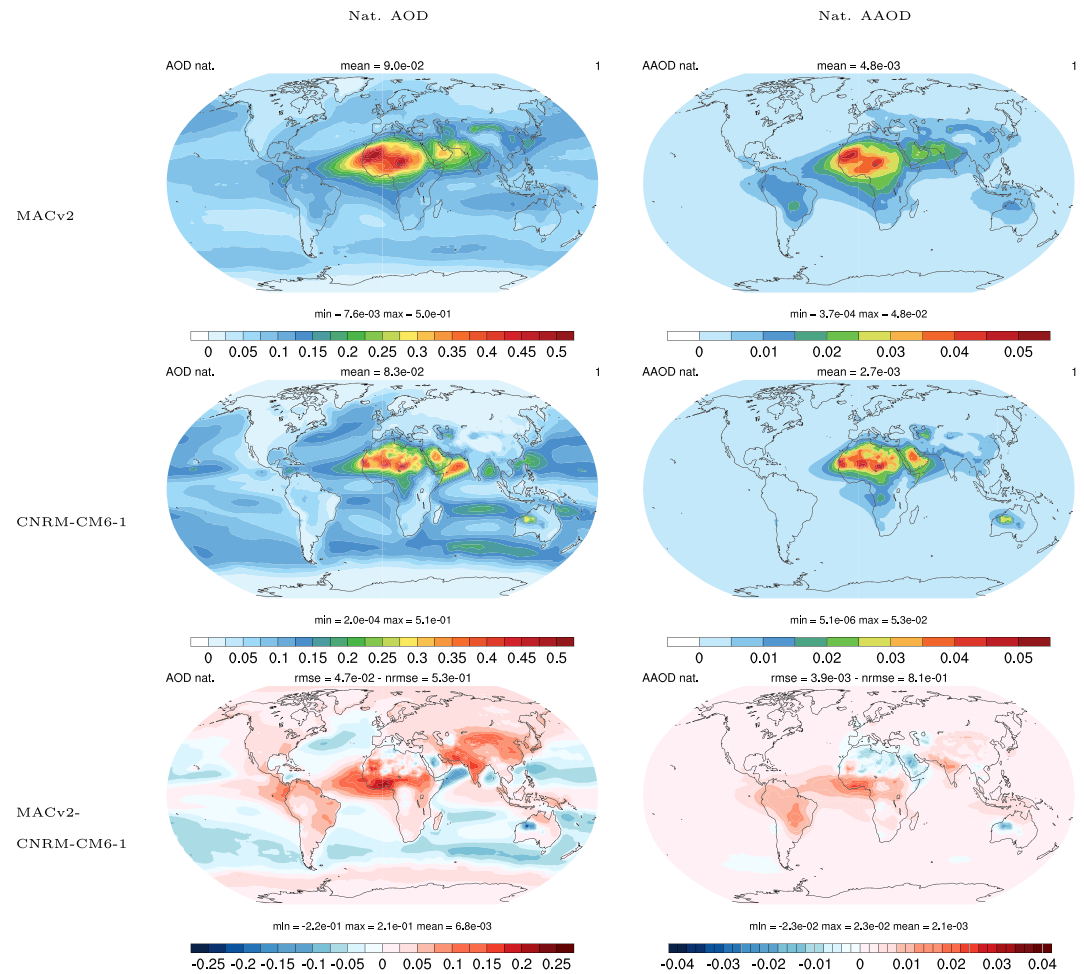


Figure 3. Mean annual AOD and AAOD around 2005 of natural aerosols. From first to last lines MACv2, CNRM-CM6-1, and difference MACv2-CNRM-CM6-1. Means of 2000–2009 for CNRM-CM6-1 and 2005 for MACv2 fields.

largest over South America and may be linked to inaccurate optical properties of biomass burning particles. Recent in situ observations over the main biomass burning regions, obtained in the frame of the ORACLES (Southern Atlantic; Zuidema et al., 2018) and SAMBBA (South America; Johnson et al., 2016) experiments, reveal SSA of about 0.85 and between 0.80 and 0.88, respectively. The BC emissions and the assumption of external mixing state (Cappa et al., 2012), as well as the absence of brown carbon particles (Zhang et al., 2019), could possibly explain part of the TACTIC_v2 SSA overestimation for smoke aerosols. In contrast, SSA values are the closest over the Southern ocean and the Sahara, where optical properties of dust and sea-salt

Table 5
Global Area-weighted Average and Standard Deviation of Monthly AOD and AAOD for the Years Shown in Figure 1, over Land and over Ocean

Data set	AOD		AAOD	
	Land	Ocean	Land	Ocean
CNRM-CM6-1	0.100 ± 0.014	0.101 ± 0.008	0.010 ± 0.001	0.002 ± 0.000
MACv2	0.164 ± 0.029	0.103 ± 0.007	0.014 ± 0.002	0.005 ± 0.001
MERRA-2	0.180 ± 0.027	0.123 ± 0.008	0.012 ± 0.002	0.005 ± 0.001
CAMSRA	0.184 ± 0.039	0.136 ± 0.012	na	na

Note. MERRA-2 figures are from Randles et al. (2017) (supplementary Table 3); CAMSRA is the CAMS reanalysis. na = not available.

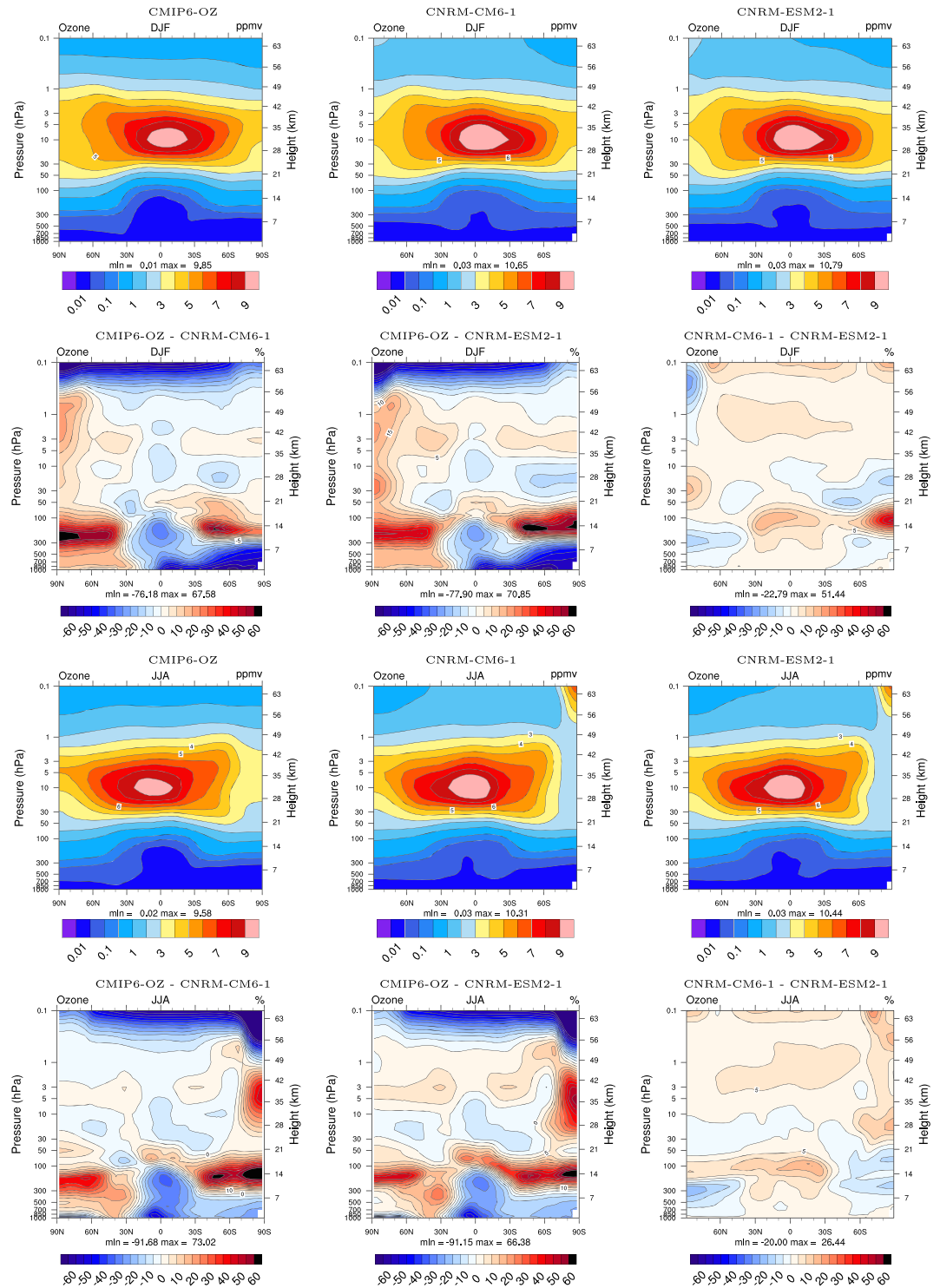


Figure 4. Mean 1990–1999 zonal ozone mixing ratio (ppmv) from 1,000 to 0.1 hPa for CMIP6-OZ and the CNRM-CM6-1 and CNRM-ESM2-1 historical ensemble simulations (see text and Table 2 for details). First two lines, DJF means with absolute values (Line 1) and relative differences (%), Line 2), and the same in last two lines for JJA.

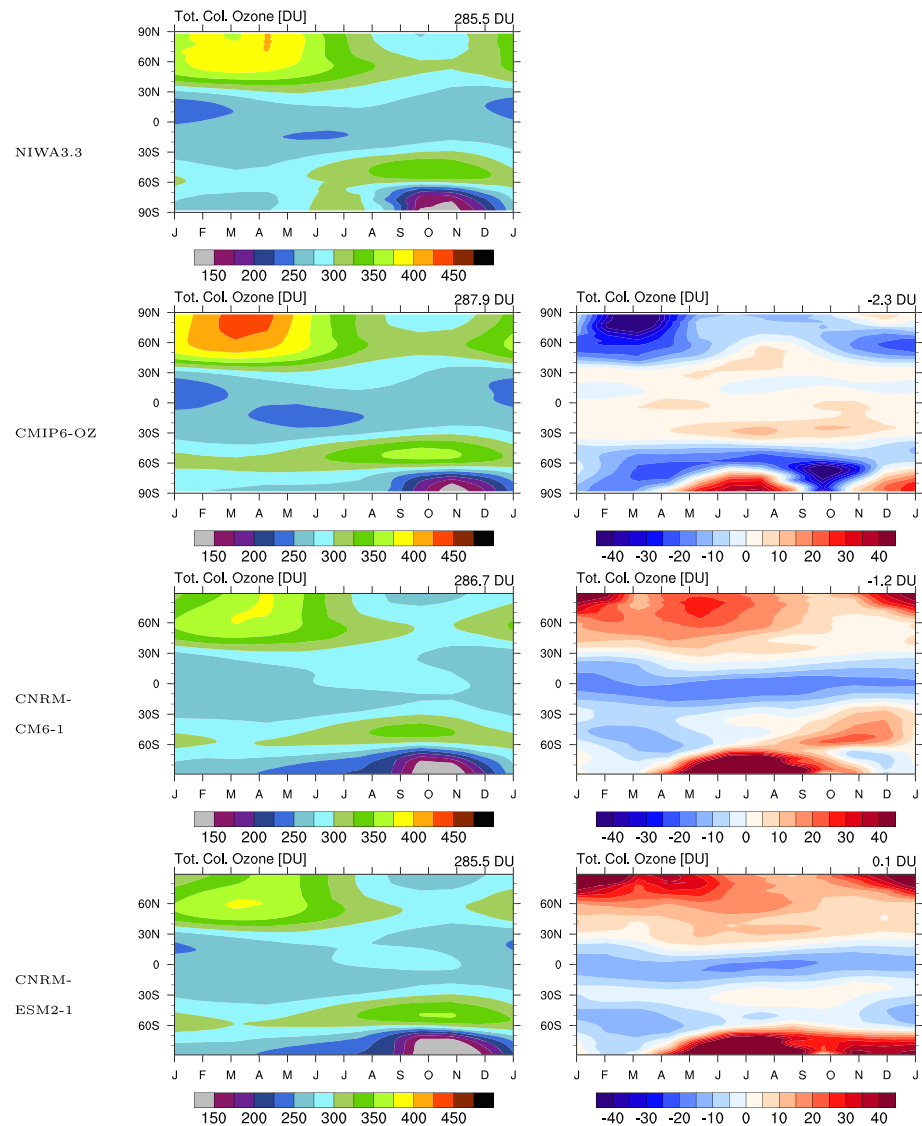


Figure 5. Monthly zonal total column ozone (DU) climatologies for 1990–1999. Lines, NIWA3.3, CMIP6-OZ, CNRM-CM6-1, and CNRM-ESM2-1. Columns, absolute values, and differences (NIWA3.3 minus XX).

aerosols are more constrained. CNRM-CM6-1 features are consistent with results presented in Lacagnina et al. (2015), which showed that models generally overestimate SSA while they underestimate AAOD. In addition, a number of characteristics of the AAOD distribution appear more realistic in MACv2 than in CNRM-CM6-1, including higher spatial variability over the oceans in part due to the transport of continental aerosols (Lacagnina et al., 2015). Most of these differences in total AAOD between MACv2 and CNRM-CM6-1 are due to differences in natural AAOD (Figure 3 and Table 5), notably over ocean where a large bias is noted, due to underestimates of transported mineral dust and biomass burning particles. It is also worth mentioning that biases of the anthropogenic AAOD are of the same order of magnitude in MACv2-SP and CNRM-CM6-1. The NRMSE of CNRM-CM6-1 is larger for AAOD than for AOD (7.2×10^{-1} vs. 5.0×10^{-1}), while those for SSA and ASY are of a smaller order of magnitude. The MACv2 ASY parameter is smaller than the CNRM-CM6-1 one over all oceans and larger over roughly a 0–30°N latitude band over the continents.

3.2. Ozone

Zonal plots of mean 1990–1999 (DJF and JJA seasons) ozone mixing ratios (mol mol^{-1}) appear in Figure 4. CNRM-CM6-1 and CNRM-ESM2-1 historical ensembles (see Table 2), as well as CMIP6-OZ, are shown, together with their relative differences. CNRM-CM6-1 and CNRM-ESM2.1 are within 10% throughout most

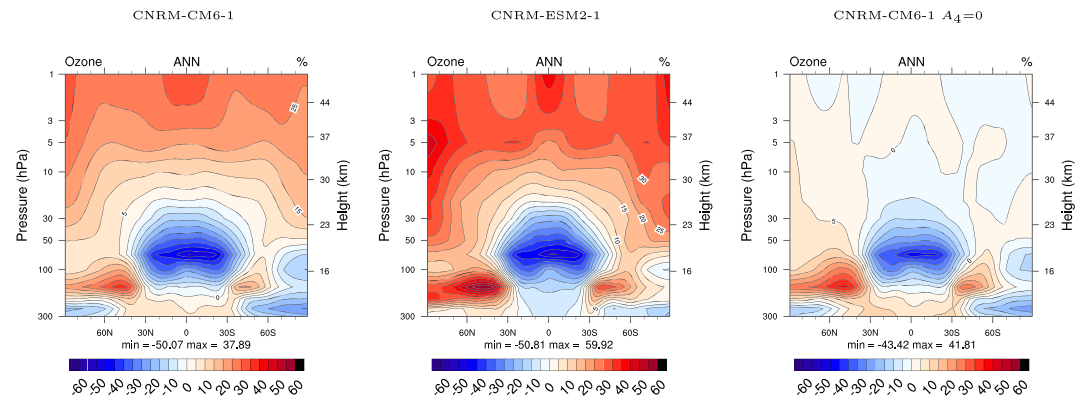


Figure 6. Zonal mean ozone percentage differences between the 4xCO₂Clim-4xCO₂ and the piClim-control simulations (last 10 years), from 300 to 1 hPa. (left) CNRM-CM6-1, (middle) CNRM-ESM2-1, and (right) CNRM-CM6-1 with the A_4 coefficient of the linear ozone scheme (see equation (4)) set to 0.

the atmosphere, with some larger differences around the tropopause and in the mesosphere. Differences are larger between the CMIP6-OZ and the CNRM ozone mixing ratios, with maximum differences in the same regions of the tropopause and of the mesosphere and near the surface. However, through the major part of the stratosphere where ozone mixing ratios are the highest, differences are smaller than 10% with the exception of the high latitudes of the winter hemisphere. In the troposphere, differences show also an annual cycle with reduced differences in JJA. In both seasons, however, the CMIP6 tropospheric ozone is higher than the CNRM-CM6-1 one in the Northern Hemisphere and smaller in the Southern Hemisphere (with biases around 15 ppb). The CNRM tropospheric ozone lacks the very marked hemispheric difference with mixing ratios higher than 40 ppb in the whole northern troposphere and mixing ratios lower than 30 ppb in the entire southern troposphere, reflecting industrialized latitudes.

Figure 5 presents the 1990–1999 monthly mean latitudinal evolution of the total column ozone (TCO) for the CMIP6-OZ data set and the CNRM-CM6-1 and CNRM-ESM2-1 historical simulations. All these three data sets are compared to the NIWA3.3 columns, as another reference data set, and the respective differences are shown. The annual cycles of the three data sets are quite similar at all latitudes, as is the latitudinal gradient. However, biases against NIWA3.3 of the CMIP6-OZ and the CNRM-CM6-1 ozone have opposite signs, with too high columns in the tropics for CNRM-CM6-1 and too low columns elsewhere especially in the 60–90°N band (see also Figure 10). The global mean of the differences is smaller for CNRM-CM6-1 (–1.2 DU) than for CMIP6-OZ (–2.3 DU) and almost null (0.1 DU) for CNRM-ESM2-1, with a reduced negative bias in the tropical band. The largest biases appear at high latitudes, in both hemispheres, and timing of the ozone depletion is better represented in CNRM-CM6-1 than in CNRM-ESM2-1 with a too long duration in CNRM-ESM2-1.

4. Sensitivity to CO₂ and Historical Evolutions

4.1. Tracking the Response of the Ozone and Aerosol Schemes to Rising CO₂

With the description and the PD evaluation of the various aerosols and ozone schemes completed, we now investigate how these schemes may interact with climate change. For this goal, we use a well-established global-scale climate metric, the Equilibrium Climate Sensitivity (ECS), namely, the global mean surface-air temperature response to an abrupt doubling of CO₂ relative to the PI. The use of this idealized approach has the advantage of constraining the role of anthropogenic forcing agents other than CO₂, such as greenhouse gases, aerosols, and land-cover changes.

The first objective of the simulations analyzed in this paragraph is to evaluate whether the linear ozone scheme is responding correctly in an abrupt-4xCO₂ experiment. Indeed, one could be concerned from equation (4) that evolution of ozone in this simulation, with all monthly coefficients of the linear scheme fixed at their 1850 value, would not match the atmospheric changes due to the quadrupling of CO₂ and would, for instance, result in nonphysical high ozone in the upper troposphere with the rising of the tropopause. An excess in upper-tropospheric tropical ozone leads to increased water entry into the stratosphere, all this in the end increases the ECS (Nowack et al., 2015). The second objective is to assess if and

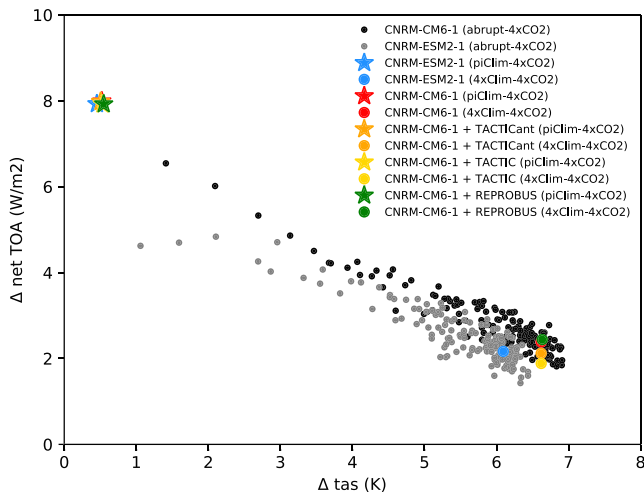


Figure 7. Gregory et al. (2004) type plot, x axis change with the corresponding pi-Control simulation in global average surface temperature, y axis change in net downward radiative flux. CNRM-CM6-1 CMIP6 abrupt-4xCO2 (black dots) and CNRM-ESM2-1 CMIP6 abrupt-4xCO2 (gray dots). All other colored dots are 20 year mean changes from piClim-type simulations (fixed SST). “4xClim-4xCO2”: 4xCO2Clim-4xCO2 simulations. See text for additional details.

how much the difference in ECS between CNRM-CM6-1 and CNRM-ESM2-1 (5.06 and 4.55 K, respectively; see Séférian et al., 2019) is related to the representation of ozone and of aerosols.

For those purposes, triplets of 20 year long SST forced simulations (piClim-control, piClim-4xCO2, and 4xCO2Clim-4xCO2), along the lines described in Andrews et al. (2015) and Ringer et al. (2014), have been performed with several configurations of the model. The 4xCO2Clim-4xCO2 simulations have SST and sea-ice conditions of a 30 year mean monthly climatology from the abrupt-4xCO2 simulations. The various configurations consist in (1) a CNRM-ESM2-1 one, (2) CNRM-CM6-1 ones with the ozone linear scheme either as in equation (4) or with one or several coefficients of the linear ozone scheme set to zero, (3) CNRM-CM6-1 with the chemistry scheme REPROBUS-C_v2, and (4) CNRM-CM6-1 with the aerosol scheme TACTIC_V2, either for all aerosols or for anthropogenic aerosols only (in the latter case, monthly AODs of DD and SS are prescribed).

Figure 6 illustrates the mean relative change in ozone mixing ratios (mean over last 10 years of the simulations) between 4xCO2Clim-4xCO2 and piClim-control, for CNRM-CM6-1 (and the linear ozone scheme) and CNRM-ESM2-1. Spatial distribution and intensity of these changes look very similar over all tropical latitudes and most of the stratosphere. They agree to expected changes in ozone under abrupt-4xCO2 experiments

(see, for instance, Nowack et al., 2018). Setting the A_4 coefficient (dependence of ozone evolution to temperature) to 0 resulted in a very different ozone field under 4xCO2Clim-4xCO2 conditions through most of the stratosphere, with smaller evolutions from the control simulation than those of CNRM-CM6-1 (see Figure 6). The dependence to the A_6 coefficient (not shown) is of less importance than the dependence to A_4 , but it, however, plays a role in ensuring a correct distribution of ozone, particularly in the middle to upper stratosphere at midlatitudes. We conclude from this short analysis on the satisfactory behavior of the ozone representation in CNRM-CM6-1 abrupt-4xCO2 experiments.

Figure 7 is a Gregory et al. (2004) type plot in which the regression of the change in net TOA radiation (ΔN) against the change in surface temperature (Δt_{as}) gives an estimate of the ECS in the case of 4xCO2 perturbed simulations ($ECS = 0.5 \times \Delta t_{as}$ intercept when $\Delta N = 0$ and $\Delta N = F - \lambda \Delta t_{as}$, with λ the climate feedback parameter and F the radiative forcing. In addition to the yearly dots of the CNRM-CM6-1 and CNRM-ESM2-1 CMIP6 abrupt-4xCO2 experiments (black and gray small dots, respectively), Figure 7 includes colored dots. For a given color, a star reflects changes in TOA fluxes under 4xCO2 conditions corresponding to the beginning of the abrupt-4xCO2 simulation, while a large colored dot reflects changes corresponding to its end. Therefore, both points enable also to estimate the ECS of the model in a given configuration.

Figure 7 shows that as the CNRM-CM6-1 red and green dots almost overlap, the ECS values of CNRM-CM6-1 with the linear scheme and with the REPROBUS-C_v2 scheme are very similar. Table 6, which provides the numbers associated with the various SST-forced regression lines in Figure 7, confirms this statement.

Table 6
Parameters of the Various Regression Lines in Figure 7, T_{eq} (K) Intercept With $y = 0$, λ ($W \cdot m^{-2} \cdot K^{-1}$), F ($W m^{-2}$) (See Text for Details)

Simulation	T_{eq}	λ	F
CNRM-ESM2-1	8.21	1.02	8.39
CNRM-CM6-1	9.20	0.92	8.47
CNRM-CM6-1 + TACTICant	8.80	0.96	8.46
CNRM-CM6-1 + TACTIC	8.50	0.99	8.45
CNRM-CM6-1 + REPROBUS	9.30	0.90	8.42

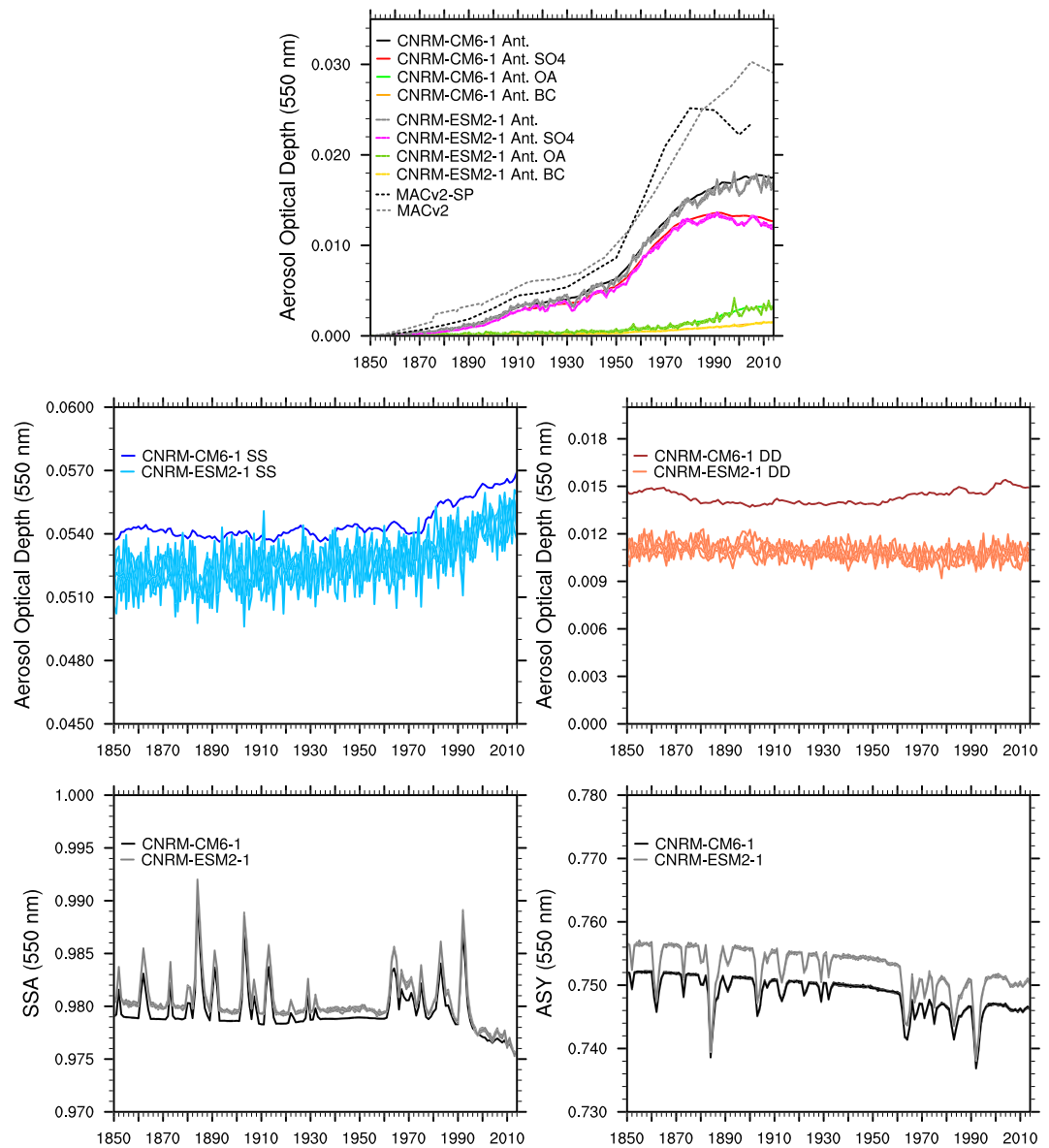


Figure 8. Time series between 1850 and 2014 of yearly global mean aerosol optical properties. First line anthropogenic AODs, including biomass burning, for MACv2, MACv2-SP, and CNRM-CM6-1 and CNRM-ESM2-1 CMIP6 historical simulations. The three anthropogenic aerosol types of TACTIC_v2 (BC, OM, and SO₄) are also presented. Second and third lines show outputs from CNRM-CM6-1 and CNRM-ESM2-1 CMIP6 historical simulations. (second line) SS AODs (left) and DD AODs (right). (third line) SSA (left) and ASY (right) of total aerosols.

On the contrary, the ECS of CNRM-CM6-1 with TACTIC_v2 (yellow) is noticeably different from that of CNRM-CM6-1 (red) and quite close to the ECS of CNRM-ESM2-1 (blue). Several candidates could explain these results, such as the overall aerosol content that is different in CNRM-CM6-1 and in CNRM-ESM2-1 with TACTIC_v2 because of differences in natural aerosols or the vertical distribution of aerosols that change at each time step of the physics when TACTIC_v2 is activated. The additional group of simulations, CNRM-CM6-1 with TACTIC_v2 for anthropogenic aerosols (CNRM-CM6-1 + TACTICant, orange dots), allows to confirm that aerosols feedbacks, that is, changes of natural aerosols due to changes in meteorology (see simulations CNRM-CM6-1 + TACTIC and CNRM-CM6-1 + TACTICant), are slightly smaller, but comparable, than feedbacks in link with the interactivity of aerosols (see simulations CNRM-CM6-1 and CNRM-CM6-1 + TACTICant).

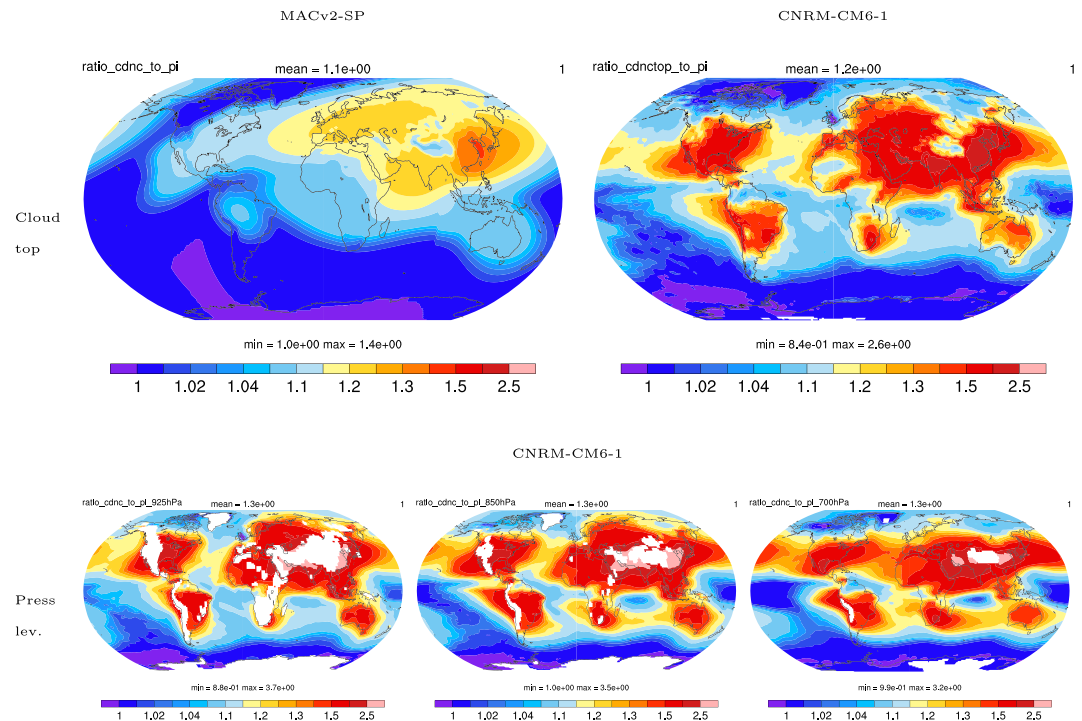


Figure 9. Proportional change in CDNC between 2000 and 1850, with scale as in figure 12 of Stevens et al. (2017). (first line) MACv2-SP and CNRM-CM6-1 amip-hist-aod simulation (see text for details) at cloud top. (second line) amip-hist-aod at 925, 850, and 700 hPa.

4.2. Evolution of Aerosol Optical Properties

At this stage of the paper, we remind the reader that differences in CNRM-CM6-1 and CNRM-ESM1-1 aerosols may be due, in particular, to differences in meteorology (CNRM-CM6-1 aerosols are those of an AMIP-type simulation, while CNRM-ESM2-1 historical simulations include coupling with the ocean) and also to differences in land cover as CNRM-ESM2-1 considers anthropogenic land use changes that impact land cover characteristics. Figure 8 shows AOD time series between 1850 and 2014, with separate plots for anthropogenic and natural aerosols. Trends of the annual global mean anthropogenic AODs (first line) are comparable in MACv2, MACv2-SP, and CNRM models over 1850–1950 but then are smaller for the CNRM models over 1950–1980. This trend is scaled in MACv2-SP on the CMIP6 SO₂ and NH₃ anthropogenic emissions (Hoesly et al., 2018; Stevens et al., 2017), while in CNRM-CM6-1, it reflects both sources and sinks of the anthropogenic aerosols of TACTIC_v2 (SO₄, BC, and OM). Flato et al. (2013) note that despite the use of common anthropogenic aerosol emissions for the historical simulations, ACCMIP models (17 in total) show very different trends in aerosol loading since 1850. Variability of the sinks resulting from model internal variability appears in the CNRM-ESM2-1 outputs (five realizations of CMIP6 historical simulations). This variability appears small with regard to the overall trend, and the time series of CNRM-CM6-1 and CNRM-ESM2-1 anthropogenic aerosols coincide, both for total anthropogenic aerosols and for their individual components.

Differences in the level of natural aerosols between MACv2 and CNRM-CM6-1 (not shown) are around 10% and lower at the end of the period. Indeed, the MACv2 AOD of natural aerosols remains constant (global mean of 0.09), whereas CNRM-CM6-1 AOD of sea-salt aerosols increases by about 5%, both due to an increase in winds over some equatorial regions and over the southern ocean and to an increase in SST. There is no such noticeable increase in the CNRM-CM6-1 dust aerosols. Another interesting feature is that in CNRM-CM6-1, the level of the sum of BC, OM, and SO₄ aerosols in 1850 (not shown) is almost as high as the level of dust aerosols (respective AOD of 0.012 and 0.014), although their spatial distributions are different. Lower SS and DD AODs in CNRM-ESM2-1 than in CNRM-CM6-1 throughout 1850–2014 denote the influence of the climate on emissions of these compounds. For the DD aerosols, emissions have also been lowered because of a smaller fraction of bare soil due to the use of the CMIP6 Land used Harmonized data

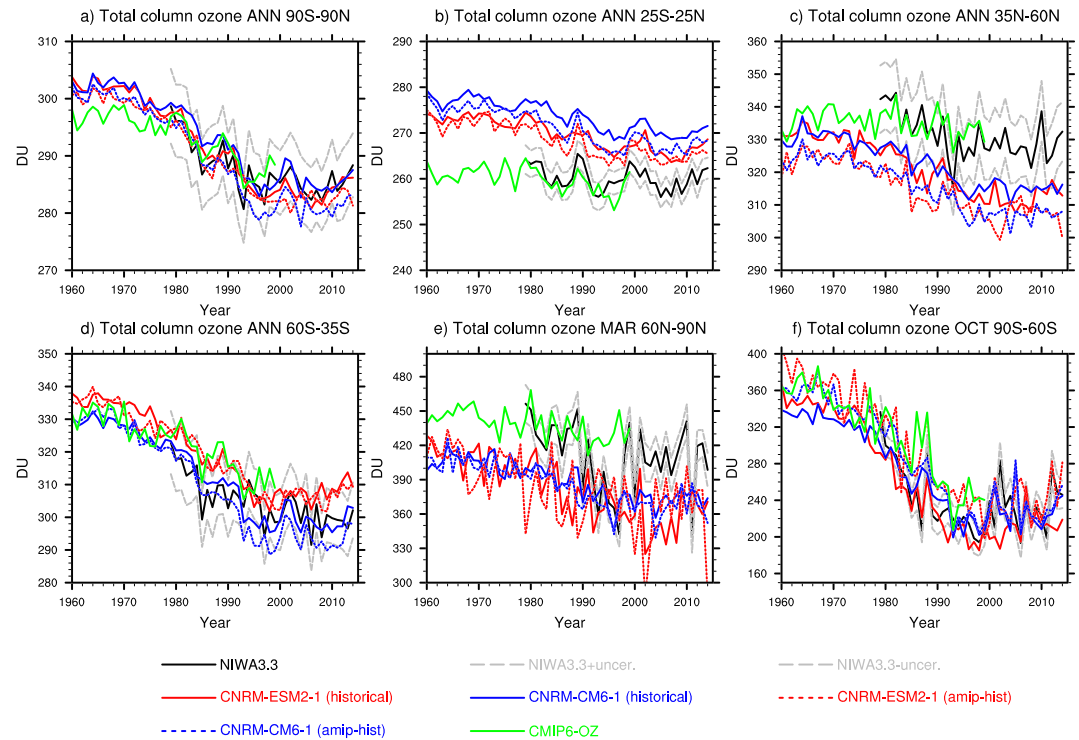


Figure 10. Time series of area-weighted total column ozone from 1960 to 2014 for the annual mean for different latitude bands (a to d) and for March and October in (e) and (f) (as in Eyring et al., 2013). Data sets presented here are NIWA3.3 (in black, \pm uncertainty in gray), CMIP6-OZ (in green), CNRM-CM6-1 ensembles (in blue), and CNRM-ESM2-1 ensembles (in red). For the CNRM models, full lines for CMIP6 historical ocean-atmosphere simulations and dotted lines for CMIP6 amip-hist simulations.

(see <http://goo.gl/r8up31>). The interannual variability of the dust aerosol AOD in CNRM-ESM2-1 is larger than the one of the sea-salt aerosols ($\approx 5\%$ vs. $\approx 2\%$ relative standard deviations, respectively), and they are both comparable to the interannual variability of their respective emissions (not shown). Impact of aerosol composition on total aerosols results in very small variations in the global ASY or SSA parameters between 1850 and 2014 (0.5% and 0.3% for the relative standard deviations, respectively). The main peaks in these two parameters are related to volcanic eruptions that brought stratospheric aerosols with higher SSA (0.999) and lower ASY (0.72). The weak historical trend in SSA and ASY is related to the increase in anthropogenic aerosols. Note that the MACv2-SP data set does not consider anthropogenic aerosol composition changes over time. The $\frac{Nat.aerosols}{Anthro.aerosols}$ ratios for CNRM-CM6-1 and MACv2 are close, 25% versus 30%, respectively.

4.3. Aerosol-Cloud Interactions

As the only indirect effect represented in CNRM-CM6-1 is the Twomey effect, the change in CDNC between PI and PD can be seen as a relevant proxy of the anthropogenic aerosol-cloud interactions in CNRM-CM6-1. This change in CDNC has been calculated from a pair of dedicated 10 year fixed SST CNRM-CM6-1 simulations with interactive aerosols, one with 1850 static anthropogenic aerosol emissions (PI) and one with 2000 emissions (PD). Ratios of CDNC between PD and PI simulations are shown in Figure 9 for the MACv2-SP dataset and CNRM-CM6-1 at the cloud top, as well as at various pressure levels (950, 800, and 700 hPa) for CNRM-CM6-1 only. Although the magnitude of the change depends on the altitude to a certain extent, at all levels, the largest changes in CNRM-CM6-1 appear over Asia in agreement with changes in MACv2-SP (see equation 15 of Stevens et al., 2017, and Figure 9). Two features however are clearly different between CNRM-CM6-1 and MACv2-SP. First, the CNRM-CM6-1 ratios show areas of doubling or more CDNC between PI and PD, especially over continents, while the MACv2-SP ratios are limited to 1.37. This results in a lower global mean value (1.07) for MACv2-SP than for CNRM-CM6-1 (1.20). The relatively low value in MACv2-SP is discussed in Stevens et al. (2017) and seems also to be low compared to a number of observations; McCoy et al. (2017) report that the change is estimated to be larger than three over highly polluted regions such as China. Second, since the MACv2-SP data set is derived from satellite observations which

only see clouds at their top, the MACv2-SP CDNC is independent from the model level and is more representative of the cloud top properties. This assumption has been adopted in the parameterization of this field in certain climate models (Quaas et al., 2006). In reality, CDNC at the cloud top is smaller than inside the cloud due to cloud entrainment (Zeng et al., 2014). In CNRM-CM6-1, the mean change in CDNC from PI to PD is maximum at 850 hPa. Finally, uncertainties in this CNRM-CM6-1 CDNC change might be related to the (Menon et al., 2002) formulation itself that could be questioned when used in high aerosol loadings or in PI conditions.

4.4. Evolution of Ozone

As there is no trend in the evolution of the historical TCO of CNRM-ESM2-1 prior to 1960 (not shown), Figure 10 shows this evolution over the period 1960–2014. Although tropospheric ozone weights only about 10% of the TCO, we emphasize again that we do not model the increase in tropospheric ozone related to the increase in emissions of ozone precursors. Hence, changes in the CNRM-CM6-1 and CNRM-ESM2-1 tropospheric ozone are only due to changes in upper tropospheric and stratospheric ozone and follow the evolution of stratospheric ozone.

Figure 10 shows 1960–2014 time series of TCOs as modeled in CNRM-CM6-1 and CNRM-ESM2-1 CMIP6 coupled (historical ensembles; see Table 2) and forced (amip-hist ensemble of 10 members for CNRM-CM6-1 and 1 member only for CNRM-ESM2-1) simulations, averaged over various latitude bands, and different periods of the year (annual mean, March, and October). The CMIP6-OZ data set is also shown, as is the NIWA3.3 data set to get further insight in the CNRM performance. In general, the CMIP6 and NIWA3.3 TCO compare relatively well, except however in 1990–1999 60–90°N (see Figures 10e and 5).

Averaged over 90°S to 90°N (see Figure 10a), CNRM TCOs are higher than CMIP6-OZ TCO over 1960–1980 (~5 DU), in link with higher TCOs over the tropical band (~15 DU; see Figure 10b). After 1980, all evolutions are within the uncertainty of NIWA3.3 (gray lines), reflecting a correct trend over 1980–2000 driven by the trends in the southern latitudes (Figures 10d and 10f). In the tropical band, the CNRM positive bias is smaller for CNRM-ESM2-1 than for CNRM-CM6-1, but the modulation of the CNRM TCOs by the solar cycle are too weak. In contrast, in the 35–60°N and 60–90°N bands (Figures 7c and 7e), CNRM TCOs are too low, again outside of the uncertainties of NIWA3.3. These negative biases could be the signature of a too weak Brewer-Dobson circulation, but as there is an excess of ozone in the model in the 60–35°S band (Figure 7d), this affirmation could be modulated, keeping in mind the intrinsic hemispheric differences in the stratospheric transport. In the 60–90°N band (Figure 7e), the interannual variability of the CNRM-ESM2-1 historical ensemble (red full line) is closer to that of NIWA3.3 than the variability of both CMIP6-OZ data (green line) and CNRM-CM6-1 historical ensemble (blue full line). In the 60–90°S band, ozone depletion of the CNRM models is within the uncertainty of the observations, with the 2000–2005 higher columns better represented by CNRM-CM6-1. Finally, TCOs of the CNRM coupled (ocean-atmosphere) and forced (atmosphere only, dotted lines) simulations differ, with generally higher TCOs in the coupled simulations (e.g., Figures 10a and 10c).

5. Aerosol and Ozone Forcings

5.1. Forcing Calculations

In order to estimate the aerosol and ozone forcings over the historical period, we have calculated their respective ERFs. The aerosol ERF can be differentiated between aerosol-radiation interactions (ERF_{ari}) and aerosol-cloud interactions (ERF_{aci}). Anthropogenic aerosol ERF_{ari} and ERF_{aci} can be computed as in Ghan (2013). ERF_{ari} is thus defined as $\Delta(F - F_{\text{clean}})$, where Δ refers to the difference between an aerosol-perturbed simulation and a PI control simulation, F to the TOA radiation flux (net, SW, or LW) and F_{clean} to the TOA radiation flux (net, SW, or LW) neglecting both scattering and absorption by aerosols. Ghan (2013) compute ERF_{aci} as $\Delta(F_{\text{clean}} - F_{\text{clear, clean}})$, where $F_{\text{clear, clean}}$ is the TOA radiative flux neglecting scattering and absorption by both clouds and aerosols. Other techniques to estimate ERF_{ari} and ERF_{aci} could lead to slightly different estimates, but Zelinka et al. (2014) emphasize that the technique of Ghan (2013) is the most accurate one. Total anthropogenic aerosol ERF then is written as

$$\text{ERF} = \text{ERF}_{\text{ari}} + \text{ERF}_{\text{aci}} + \text{ERF}_{\text{res}},$$

where ERF_{res} is a residual term defined as $\Delta(F_{\text{clear, clean}})$ and representing mainly the change in surface albedo (Ghan, 2013). All these terms are issued from multiple calls to the climate model radiation scheme

Table 7

Summary of RFMIP and/or AerChemMIP Fixed SST Simulations Used to Calculate the ERF of Aerosols With CNRM-ESM2-1 (Noted ESM2-1 in This Table) and CNRM-CM6-1 (noted CM6-1 in This Table)

Simulations	MIP	Model	Period	SO ₄ , BC, OM	DD, SS
piClim-control	RFMIP/AerChemMIP	CM6-1	30 years	1850 CM6-1 AOD	1850 CM6-1 AOD
piClim-control	RFMIP/AerChemMIP	ESM2-1	30 years	emis. 1850	int.
piClim-aer	RFMIP/AerChemMIP	CM6-1	30 years	2014 CM6-1 AOD	2014 CM6-1 AOD
piClim-aer	RFMIP/AerChemMIP	ESM2-1	30 years	emis. 2014	int.
piClim-TYPE	AerChemMIP	ESM2-1	30 years	2014 for TYPE emis. only	int.
piClim-2xEMIS	AerChemMIP	ESM2-1	30 years	1850 with double emis. for EMIS	int.
histSST	AerChemMIP	ESM2-1	1850–2014	trans. emis 1850–2014	int.
histSST-piNTCF	AerChemMIP	ESM2-1	1850–2014	emis. 1850	int.

Note. All piClim* simulations have forcings set to 1850 values, except for aerosols when specified above. int. for interactive TACTIC aerosols. TYPE refers to the following species: SO₂, BC, and OM. EMIS refers to the following emissions: dust, DMS, SS, and fire.

whereby the model radiation scheme is called several times consecutively with one or more radiative species set to a different value.

ERFari and ERFaci have been calculated with two protocols, along the lines of the AerChemMIP protocols (Collins et al., 2017). One protocol is the one of the CMIP6 fixed-SST piClim simulations to derive PD ERFs; Forster et al. (2016) indicate that in this method, the 5–95% confidence level of the global ERF is reduced to 0.1 W m⁻² for 30 year integrations. The second protocol is used to derive transient ERFs; the corresponding CMIP6 simulations are the so-called histSST/histSST-piNTCF ones (see Table 7). In addition to RFMIP and/or AerChemMIP piClim-type simulations (see Table 7), we performed additional piClim-type simulations in order to disentangle different aspects of the anthropogenic aerosol ERF. Table 8 summarizes the characteristics of these simulations with regard to their aerosol forcing, separating anthropogenic and natural aerosols. CNRM-CM6-1 and CNRM-ESM2-1* use prescribed aerosol AODs, and all piClim-aerxx simulations come along with a corresponding piClim-controlxx simulation. The objectives here are to estimate, in the anthropogenic aerosol ERF, the impact of the interactivity of aerosols, the impact of the natural aerosols, and the impact of the configuration of the model (atmosphere-ocean general circulation model vs. ESM).

As far as the ozone forcing is concerned, previous studies have derived it from calculations with off line radiative codes (e.g., Checa-Garcia et al., 2018; Cionni et al., 2011; Szopa et al., 2013). However, in the present work, we chose to compute differences in radiative fluxes at the TOA from pairs of simulations, along the protocols defined by AerChemMIP and RFMIP, even though there was a possible weakness of these protocols owing to the small amplitude of the signal (Forster et al., 2016; Myhre, Shindell, et al., 2013). This

Table 8

Summary of Supplementary Fixed SST Simulations Used to Calculate the ERF of Aerosols With CNRM-ESM2-1 (Noted ESM2-1 in This Table) and CNRM-CM6-1 (Noted CM6-1 in This Table)

Simulations	Model	Period	SO ₄ , BC, OM	DD, SS
piClim-aerYY	ESM2-1	30 years	YY emis	int.
piClim-aerant	CM6-1	30 years	2014 CM6-1 AOD	1850 CM6-1 AOD
piClim-controlAODCM	ESM2-1*	30 years	1850 CM6-1 AOD	1850 CM6-1 AOD
piClim-aerAODCM	ESM2-1*	30 years	2014 CM6-1 AOD	1850 CM6-1 AOD
piClim-controlAODESM	CM6-1	30 years	1850 ESM2-1 AOD	1850 ESM2-1 AOD
piClim-controlAODESM	ESM2-1*	30 years	1850 ESM2-1 AOD	1850 ESM2-1 AOD
piClim-aerAODESM	CM6-1	30 years	2014 ESM2-1 AOD	1850 ESM2-1 AOD
piClim-aerAODESM	ESM2-1*	30 years	2014 ESM2-1 AOD	1850 ESM2-1 AOD

Note. ESM2-1* indicates the use of CNRM-ESM2-1 without the interactive aerosol scheme. All piClim* simulations have forcings set to 1850 values except for aerosols when specified above. YY takes the following values: 1900, 1950, 1970, 1990, and 2000.

Table 9
Summary of Fixed SST Simulations Used to Calculate the ERF of Ozone With CNRM-CM6-1

Simulations	MIP	Model	Period	Ozone
piClim-control	RFMIP/AerChemMIP	CM6-1/ESM2-1	30 years	1950 (=1850)
piClim-stratO3	Supplementary	CM6-1	30 years	2014
piClim-histstratO3	Supplementary	CM6-1	65 years	Transient 1950–2014
amip-hist (3 members)	GMMIP	CM6-1	1950–2014	Transient 1950–2014
amip-hist-1950stratO3 (3 members)	Supplementary	CM6-1	1950–2014	1950 (=1850)

Note. piClim* simulations have forcings set to 1850 values except for ozone.

stratospheric ozone ERF has been diagnosed from a pair of simulations of CNRM-CM6-1, the baseline being the official piClim-control CMIP6 simulation and the second simulation being piClim-stratO₃ (see Table 9), which is identical to piClim-control except for the ozone coefficients fixed to their 2014 value. This simulation is not an official AerChemMIP simulation. A number of other simulations have been performed to diagnose the transient (1950–2014) ERF due to ozone. Table 9 provides a summary of these additional CMIP6 AMIP-type simulations, together with their respective reference simulation and the corresponding protocol.

5.2. PD Forcing

5.2.1. Aerosols

Figure 11 shows various aspects of the PD aerosol ERF computed from the CNRM-CM6-1 piClim-aer (and piClim-control) simulation. It should be noted that by construction, all aerosols in CNRM-CM6-1 piClim-aer are those of 2014, including the sea-salt and dust ones. Therefore, the ERF presented include aspects of natural aerosol changes between 1850 and 2014 (see also section 4.2). An additional piClim-aer type simulation has been performed, named piClim-aerant, in which the natural aerosols are fixed to 1850, whose main results are shown below in Table 10, together with results of the CNRM-ESM2-1 piClim-aer simulation. In CNRM-ESM2-1 piClim-aer, the interactive sea-salt and dust aerosols should be very close to those of the corresponding piClim-control simulation, as SSTs and land surface are the same in both simulations (1850 conditions).

The mean total ERF (LW + SW) is -1.16 W m^{-2} , dominated by the ERF_{aci} term (-0.79 W m^{-2}). The spatial distribution reveals larger heterogeneity in the southern oceans, largely due to aerosol-cloud interactions. In the Northern Hemisphere, the negative forcing over Southeast Asia appears clearly, mostly due to the ERF_{ari} term. ERF_{ari} is larger over source regions, negative over Asia, and positive over desert areas. The LW ERF (global mean > 0), quite heterogeneous, is an order of magnitude smaller than the SW ERF (global mean < 0), and the mean global residual term ERF_{fres} is more than half the LW ERF mean. DJF and JJA maps highlight the differences in the seasonal patterns, with however negative forcings in most cases over China.

Table 10 lists several simulations of the two CNRM climate models that, compared to their piClim-control corresponding simulation, enable to disentangle ERF components and total ERFs of various aerosols configurations over the period 1850–2014. More specifically, a comparison between CNRM-CM6-1 piClim-aer and piClim-aerant shows that the change in natural aerosols between 1850 and 2014 results in a change of ERF of only -0.06 W m^{-2} , compared to an ERF of -1.10 W m^{-2} for the anthropogenic aerosols. This change is mainly explained by the ERF_{ari} term. In the CNRM-CM6-1 piClim-aerAODESM simulation where monthly AODs of the anthropogenic aerosols are those derived from the CNRM-ESM2-1 simulation, the total ERF is now of -1.03 W m^{-2} to be compared to the CNRM-ESM2-1 piClim-aerAODESM ERF, -0.97 W m^{-2} . This shows the small impact of the level of natural aerosols on the anthropogenic aerosol ERF as these simulations share the same anthropogenic AODs but have a different level of natural aerosols (see Figure 8). For the sake of clarity, we repeat here that TACTIC does not take into account changes in natural aerosol other than those in DD and SS, as, for instance, changes in biogenic SOA which might vary substantially between PI and PD due to deforestation and rising temperatures. A similar small impact appears from the results of the CNRM-CM6-1 piClim-aerant and CNRM-ESM2-1 piClim-aerAODCM (total ERF of -1.10 and -1.08 , respectively). A larger difference in ERFs appears between the CNRM-ESM2-1 piClim-aer and piClim-aerAODESM, which tests the impact of the interactivity of the aerosols. Indeed, here in piClim-aer, 3-D concentrations of aerosols change at each time step of the physics, while in piClim-aerAODESM,

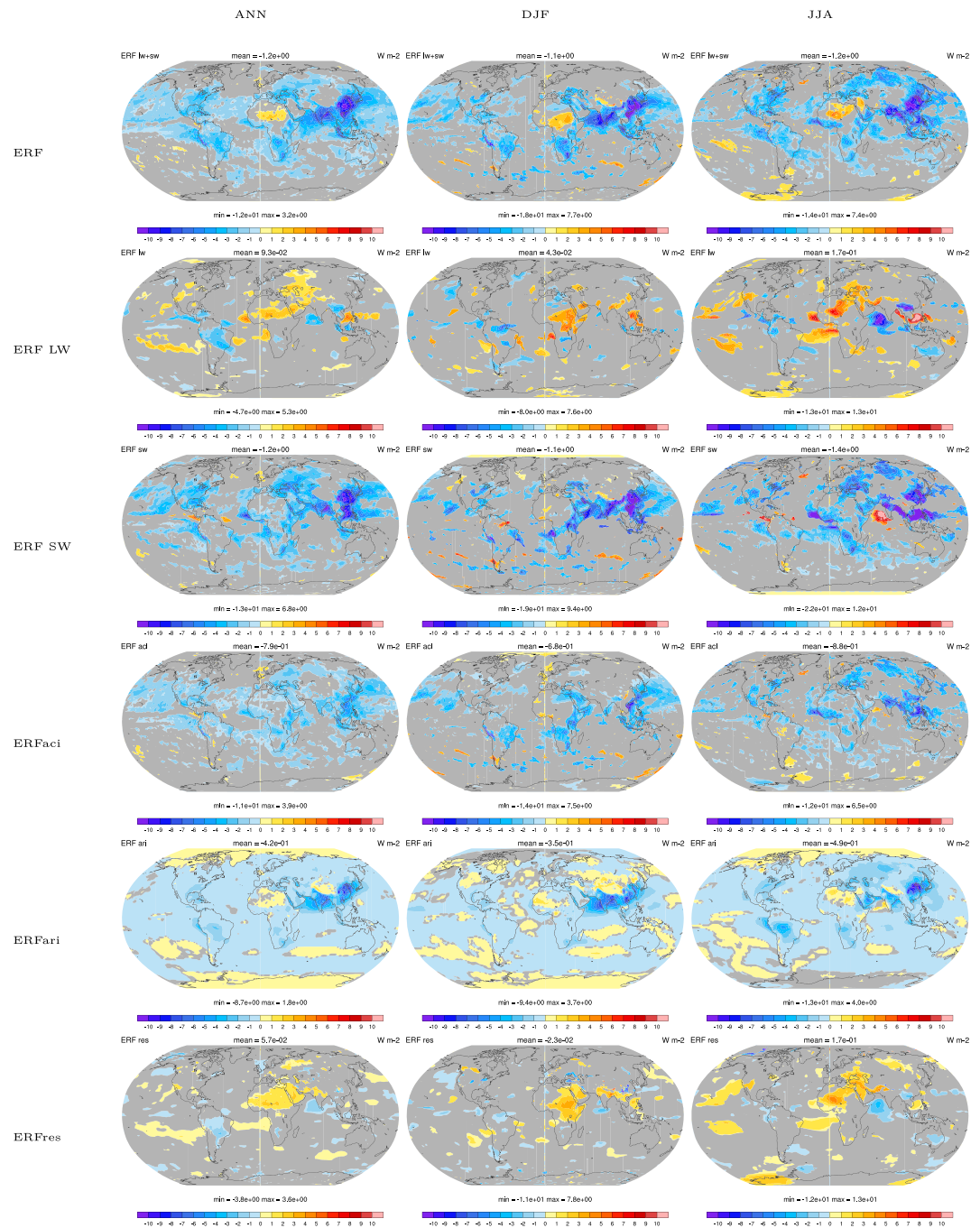


Figure 11. (lines) Components of the ERF due to the change of aerosols from 1850 to 2014 from the CNRM-CM6-1 piClim-aer simulation (30 year means). (first line) Total ERF (SW+LW), (second line) LW ERF, (third line) SW ERF, (fourth line) ERFaci, (fifth line) ERFari, and (sixth line) ERFres term (Ghan, 2013). With annual means in left column, DJF means in middle column, and JJA means in right column, areas in gray are below the 90 % level of significance using a Student's *t*-test.

monthly climatology of AODs from the piClim-aer simulation, vertically distributed by aerosol type, are considered by the radiative scheme. The total ERFs of these two simulations are, respectively, of -0.74 and -0.97 , with the largest change in ERFari (-0.21 and -0.35 , respectively). These results reveal the importance of the interactivity of the aerosols in deriving ERFs.

Simulations that test the change in an individual aerosol type indicate that the ERFari components appear relatively additive, with ERFari $\text{SO}_2 + \text{OM} + \text{BC}$ (-0.23) almost equal to ERFari in piClim-aer (-0.21).

Table 10

Aerosol ERF (in $W m^{-2}$), for the Period 1850–2014, Separated Into $ERFari^{CSSW}$, $ERFaci$, $ERFari$, $ERFres$, and total ERF ($=ERFaci + ERFari + ERFres$) for Various CNRM-CM6-1 and CNRM-ESM2-1 Simulations (ESM2-1 Indicates CNRM-ESM2-1 Without the Interactive Aerosol Scheme) Presented in Tables 7 and 8*

Simulation	Model	$ERFari^{CSSW}$	$ERFari$	$ERFaci$	$ERFres$	ERF	Ref.
piClim-aer	CM6-1	−0.63	−0.42	−0.79	0.06	−1.16	
piClim-aerant	CM6-1	−0.53	−0.36	−0.81	0.07	−1.10	
piClim-aerAODESM	CM6-1	−0.48	−0.33	−0.79	0.09	−1.03	-1.17 ± 0.30^a
piClim-aer	ESM2-1	−0.41	−0.21	−0.61	0.08	−0.74	-0.50^b
piClim-aerAODESM	ESM2-1*	−0.52	−0.35	−0.69	0.08	−0.97	
piClim-aerAODCM	ESM2-1*	−0.57	−0.39	−0.80	0.11	−1.08	
piClim-SO ₂	ESM2-1	−0.42	−0.29	−0.53	0.08	−0.75	-0.40 ± 0.20^c
piClim-OC	ESM2-1	−0.10	−0.07	−0.14	0.04	−0.17	-0.09 ± 0.07^c
piClim-BC	ESM2-1	0.10	0.13	−0.03	0.01	0.11	0.40 ± 0.40^c
piClim-2xdust	ESM2-1	0.02	0.05	−0.04	0.08	0.09	/
piClim-2xss	ESM2-1	−1.59	−1.03	−0.04	0.03	−1.04	/
piClim-2xDMS	ESM2-1	−0.10	−0.06	−0.34	0.03	−0.37	/
piClim-2xfire	ESM2-1	−0.11	−0.06	−0.20	0.03	−0.22	/

^aZelinka et al. (2014) for CMIP5 models, \pm intermodel standard deviation. ^bStevens et al. (2017). ^cMyhre, Shindell, et al. (2013) for Table 8.4 AR5 RF between 1750 and 2011 (mean and uncertainty).

On the contrary, $ERFaci$ is less additive with respect to the different aerosol species (−0.70 against −0.61). Total ERF of sulfate alone is even larger than that of the total anthropogenic aerosols (−0.75 vs. −0.74). Finally, ERFs of the natural and biomass burning aerosols are dominated by the ERF of sea salt (−1.04), followed by DMS (−0.37) and biomass burning aerosols (−0.22).

Overall, while the mean CNRM-CM6-1 total anthropogenic aerosol ERF is within the range of Zelinka et al. (2014), the mean CNRM-ESM2-1 total anthropogenic aerosol ERF appears as weak (−0.74). However, CNRM individual components $ERFaci$ and $ERFari$ are all within the range of (Zelinka et al., 2014), -0.25 ± 0.22 and -0.92 ± 0.34 , respectively. Table 10 shows also results from using the MACv2-SP parameterization in the MPI ESM (Stevens et al., 2017), where total ERF is −0.50 and $ERFari$ −0.23. Various effects explain the larger ERF in CNRM models than in MACv2-SP despite a smaller increase in anthropogenic aerosol AOD (see Figure 8). Indeed, the $ERFaci$ term is larger in CNRM models, as expected given the larger change in CDNC. In addition, the mean SSA (0.98), which affects roughly linearly the clear-sky ERF (Stevens et al., 2017), is also larger in CNRM climate models. Fiedler et al. (2019) compute a multimodel mean ERF of $-0.59 W m^{-2}$ from five Earth system models with the MACv2-SP parameterization.

As for the ERF for each aerosol species, the comparison with literature shows (1) an agreement with the large SO₄ ERF of Zelinka et al. (2014), larger than the AR5 estimate, (2) a slightly too low negative OC ERF (−0.17), and (3) a BC ERF rather at the low end of Myhre, Shindell, et al. (2013) estimates. As for the results of Myhre, Shindell, et al. (2013) for dust (-0.10 ± 0.20) and fire (-0.00 ± 0.20), they have no direct comparative value with CNRM-ESM2-1. Indeed, the latter gives ERF representing doubling dust and fire emissions, while Myhre, Shindell, et al. (2013) ones correspond to a change from 1750 to 2011.

Table 10 also reports the clear-sky SW $ERFari$ ($ERFari^{CSSW}$). As expected, the change in clear-sky flux is a negatively biased measure of $ERFari$, as a presence of clouds lessens the cooling effect of aerosols. As for the absorbing aerosols, BC, and dust, their positive $ERFari$ is slightly increased in the presence of clouds.

5.2.2. Ozone

Figure 12 shows both the change in ozone in CNRM-CM6-1 from the PI to the PD (ca. 2014, last two lines) and the corresponding ERF due to this change in ozone (first line). All plots present 30 year mean differences between the piClim-control simulation and the piClim-stratO3 simulation. The change in total ozone column is minimal in the tropical band (between 5 and 10 DU or about 3% for the annual means) and is maximal over the southern high latitudes (up to 60 DU or 22%). Separating MAM and SON plots shows the annual cycle of the ozone change, and in particular the higher ozone changes in the high latitudes of the winter hemisphere than those averaged annually (first column). Overall, if the change of ozone

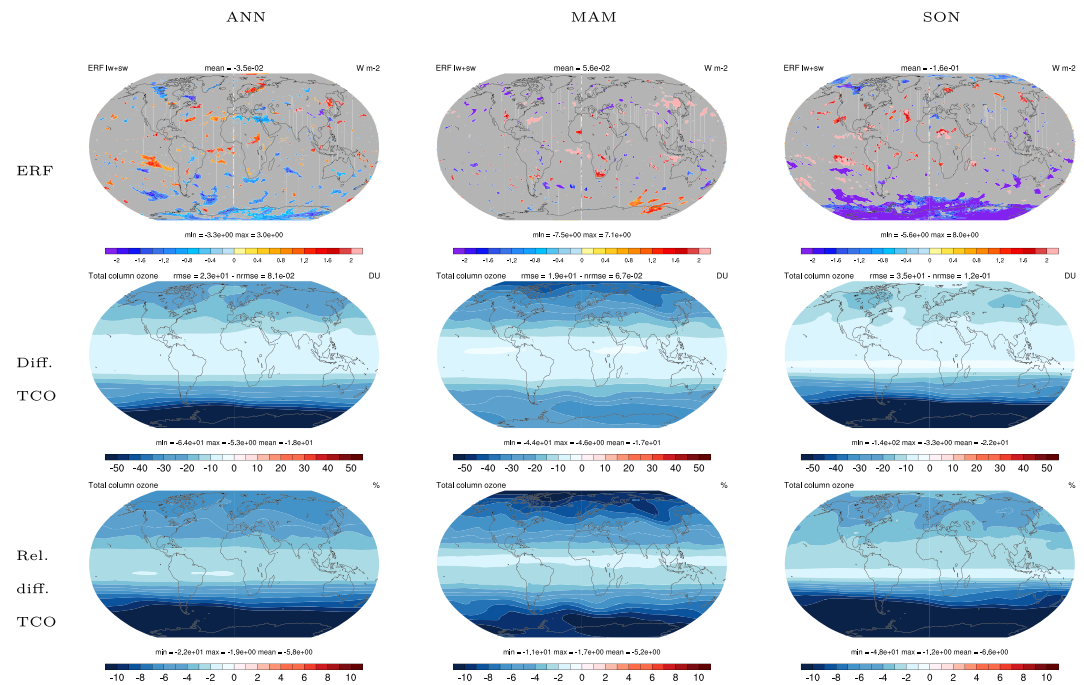


Figure 12. (first line) ERF due to ozone in CNRM-CM6-1, computed from the 30 years of the piClim-stratO3 simulation; areas in gray are below the 90% level of significance using a Student's *t*-test. (second line) Absolute difference between the 1850 (piClim-control simulation) and the 2014 (piClim-stratO3 simulation) column ozone (30 year means). (third line) The same as second line but with relative differences. Annual means on the left, MAM means in the middle, and SON means on the right.

is clear, the related ERF appears relatively noisy, with however larger continuous areas of negative ERF over areas with larger changes in ozone (i.e., high latitudes) and with a mean global value of -0.035 W m^{-2} . This is consistent with recent literature that reports mainly on the RF measure of the ozone radiative forcing, noting that the global mean ozone RF and ERF are within 10% (Shindell et al., 2013, and references therein) and that the ozone ERF is anticipated to be quite noisy (Shindell et al., 2013). According to Myhre, Shindell, et al. (2013) (see Table 8.3), the total AR5 ozone RF from 1750 to 2011 is 0.35 W m^{-2} , with a RF due to tropospheric ozone changes of 0.40 W m^{-2} (ranging from 0.20 to 0.60) and due to stratospheric ozone changes of -0.05 W m^{-2} (ranging from -0.15 to 0.05). Quite recently, the WMO scientific assessment of ozone depletion: 2018 (2018) indicate that there has been no recent update on the estimated PI to PD radiative forcing due to changes in stratospheric ozone and report only on one study, dedicated to the specific impact of short-lived ODS (Hossaini et al., 2015). However, more recently, Checa-Garcia et al. (2018) provide information of specific interest for this study as they detail both the stratospheric and tropospheric ozone forcing of the CMIP6-OZ data set, here again computed with an off-line radiative transfer model. Circa 2010, the Checa-Garcia et al. (2018) ERF of the stratospheric ozone is -0.029 W m^{-2} , with LW ERF of -0.109 W m^{-2} and SW ERF of 0.08 W m^{-2} . In CNRM-CM6-1, total ERF is -0.036 W m^{-2} , with LW ERF of 0.140 W m^{-2} and SW ERF of -0.18 W m^{-2} (see also Figure 14). Although the total (LW + SW) forcing in CNRM-CM6-1 is quite similar to that of Checa-Garcia et al. (2018), the individual LW and SW contributions are of opposite signs. The negative SW ERF in CNRM-CM6-1 can be explained by radiative transfer theory and reveals that the SW impact of the reduction of ozone in the troposphere is larger than that of the reduction of ozone in the stratosphere. The positive sign of the LW ERF could appear surprising as a reduction in ozone should lead both in the stratosphere and in the troposphere to a negative LW radiative effect (see, for instance, Iglesias-Suarez et al., 2018, and references therein). We can add that the LW ERF clear sky (not shown) presents features similar to that of the LW ERF and that the signal is quite noisy as shown in Figure 12. This change in LW ERF in CNRM simulations reflects complex interactions within the whole system.

The interannual variability computed over 30 years is of 0.121 W m^{-2} (standard deviation σ of yearly annual means), which corresponds to a 5–95% confidence interval (CI) of 0.045 W m^{-2} computed as in equation (3)

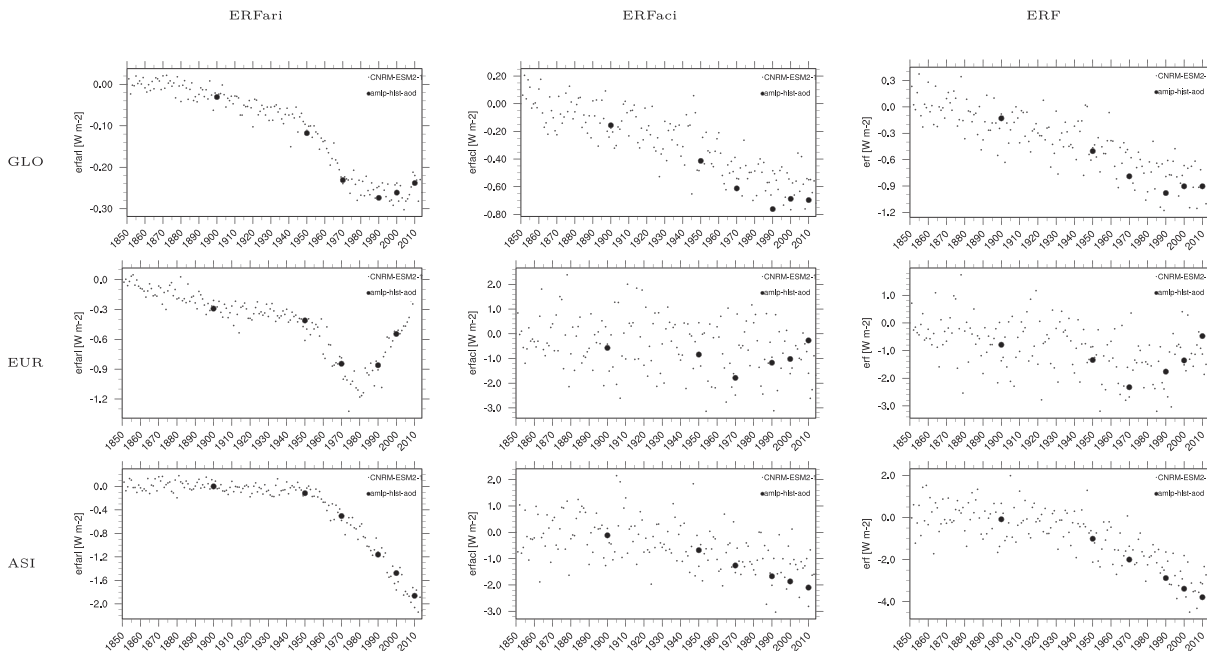


Figure 13. The 1850–2014 time series of yearly total (SW + LW) ERFari (first column), total ERFaci (second column), and total ERF (third column) for the CNRM-ESM2-1 simulations with interactive aerosols, transient simulation (CMIP6 histSST-piNTCF, small dots), or fixed forcings for given years (30 year means, amip-hist-aod, large dots). (first line) global means; (second line) means over Europe; and (third line) means over Asia (see text for details). All terms in units of $W m^{-2}$. Uncertainties on the large dots, small compared to the y axis, are not shown here but appear in Table 11.

of Forster et al. (2016):

$$CI = \frac{\sigma}{\sqrt{30}} \times t_{\text{value}},$$

where $(\sigma/\sqrt{30})$ is the standard error on the mean and t_{value} is provided by the t distribution of 29 degrees of freedom. Over 70 years of the same simulation, as recommended in Shindell et al. (2013) to diagnose the stratospheric forcing, the mean ERF is $-0.040 \pm 0.032 W m^{-2}$. These uncertainties are somehow smaller that reported in the literature, for instance, $0.07 W m^{-2}$ in Checa-Garcia et al. (2018) and Shindell et al. (2013). Forster et al. (2016) have shown that this uncertainty is largely determined by the variability of the TOA fluxes in the baseline simulation.

5.3. Historical Evolution of the Aerosol and of the Ozone Forcings

5.3.1. Aerosols

Historical values of the anthropogenic aerosol ERF have been computed from two sets of CMIP6 CNRM-ESM2-1 simulations. The first method consists in using outputs of a transient simulation (histSST-piNTCF) with all forcings fixed at 1850 levels except for the anthropogenic aerosol emissions that are the CMIP6 ones (Hoesly et al., 2018). Annual global mean values of the total ERF (SW + LW) are shown in Figure 13 (small dots). Interannual variations reveal the uncertainties in this anthropogenic aerosol ERF, much larger of course for ERFaci. The second method is based on outputs of fixed SST (1850) simulations

Table 11

Confidence Intervals ($W m^{-2}$, Minimum/Maximum) for Aerosol ERF, ERFaci, and ERFari From the Six ERF_{fSST} Simulations Shown in Figure 13

	Globe	Europe	Asia
ERF	0.07/0.08	0.23/0.29	0.28/0.37
ERFaci	0.05/0.06	0.27/0.33	0.36/0.49
ERFari	0.00/0.00	0.02/0.05	0.02/0.04

Note. Columns correspond to the three regions shown in Figure 13.

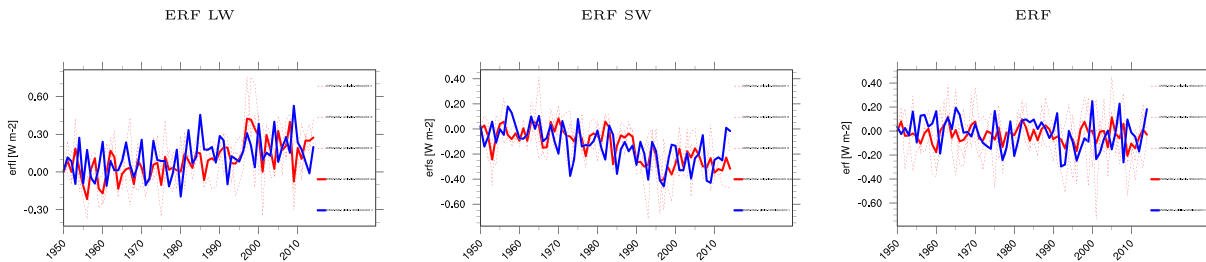


Figure 14. Time series from 1950 to 2014 of the yearly global ERF due to ozone in CNRM-CM6-1 simulations (amip-hist-1950stratO3r1, r2, r3 red dotted lines; amip-hist-1950stratO3 ensemble red thick line; piClim-1950histstratO3 blue thick line; see text for details), in the order of reading LW, SW, and LW + SW ERF.

(piClim*) repeated 30 years for specific years with their respective anthropogenic aerosol emissions. In this configuration, the sea-salt and dust aerosols are therefore always the PI ones. The 30 year mean ERF for 1900, 1950, 1970, 1990, 2000, and 2010 appear as large dots in Figure 13. The two methods provide quite consistent results. The maximum of the anthropogenic aerosol ERF occurs around 1990, with a global mean of -0.98 W m^{-2} , divided into -0.76 W m^{-2} for ERFaci and -0.27 W m^{-2} for ERFari. However, this global mean has been relatively stable from 1970 onward. Forster et al. (2016) indicate that in this ERF_{fsst} method, the 5–95% CI of the global mean ERF is reduced to 0.1 W m^{-2} . Our corresponding CIs are even smaller (see Table 11).

Trends in this 150 year period reveal distinct periods for the ERFari with ruptures in 1900, 1950, 1970, and 1990. These ruptures are less obvious for the ERFaci that shows almost no trend in the last 30 year period in agreement with results of Szopa et al. (2013). Global evolutions hide distinct regional evolutions: ERF components over Asia ($5\text{--}40^\circ\text{N}$; $60\text{--}125^\circ\text{E}$) and Europe ($5\text{--}40^\circ\text{N}$; $60\text{--}125^\circ\text{E}$) as in Szopa et al. (2013) are shown in the second and third lines of Figure 13. Differences in the evolution of ERF over these regions are striking; ERFaci over Asia also reveals a negative trend. In total, anthropogenic aerosol ERF over Asia reaches about -4 W m^{-2} .

When zooming over the 1990–2010 period as in Myhre et al. (2017), we derive changes in global mean anthropogenic aerosol ERF very comparable to those of the model multimean from Myhre et al. (2017), that is, changes of 0.08 W m^{-2} (0.1 ± 0.08) and 0.03 (0.04) for total ERF and ERFari, respectively.

5.3.2. Ozone

Figure 14 shows the 1950–2014 time series of the yearly global ERF due to ozone, computed from the simulations summarized in Table 9. The piClim-1950histstratO3 simulation follows the RFMIP protocol with transient 1950–2014 ozone and all other forcings as in the piClim-control simulation, including fixed SST and sea-ice conditions which are those of a climatology of the CMIP6 pi-Control simulation. On the contrary, the amip-hist-1950stratO3 simulations (three members) hold ozone at its PI value, with everything else as in the amip-hist corresponding simulation (AerChemMIP protocol). In addition, the ensemble of the three members is shown (red thick line). Figure 14 indicates comparable transient ERFs obtained with the two protocols, with no trend over 1950–2014 and with a smaller interannual variability ($\sigma = 0.07 \text{ W m}^{-2}$) in the amip-hist-1950stratO3 ensemble. However, as for the present ozone forcing, the separated LW and SW ERFs do not agree with what appears in literature (e.g., Checa-Garcia et al., 2018). In the CNRM simulations, LW ERF slightly increases and SW ERF slightly decreases over 1960–2010.

6. Conclusions

This paper documents characteristics of the aerosol and ozone fields of the CNRM-CM6-1 and CNRM-ESM2-1 climate models used in the course of the CMIP6 initiative. PD and historical (1850–2014) features of these fields are analyzed against reference data sets, and their respective PD and transient ERFs are discussed. These ERFs result from diagnostics of a number of CMIP6 or CMIP6-like simulations designed in the RFMIP and AerChemMIP projects.

It is important to note first that CNRM-CM6-1 and CNRM-ESM2-1 share a common physical-dynamical core and have been run with the same vertical and horizontal resolutions. Even the calibration achieved for CNRM-CM6-1 (see Voltaire et al., 2019) has been kept unchanged in CNRM-ESM2-1. CNRM-ESM2-1 adds an interactive representation of the land and ocean carbon cycle, in addition to a more complex description of the atmospheric chemistry and of the aerosols, of specific interest to this article. Second, we ensured

further consistency between the two models, notably insofar as CNRM-CM6-1 prescribed monthly AODs and monthly coefficients of the linear ozone scheme have been computed with the interactive aerosol and chemistry schemes of CNRM-ESM2-1. The main developments concerning chemistry and aerosols from previous descriptions that appear in literature concern the linear ozone scheme of CNRM-CM6-1 and the parameterization of the emissions of sea-salt aerosols in CNRM-ESM2-1.

A particular attention has been paid to compute radiative forcings in terms of ERF, as recommended in Myhre, Shindell, et al. (2013). For aerosols, the separation of ERF between ERFari, ERFaci, and a residual term (ERFres) has been carried out using the methodology of Ghan (2013) that requires an additional call to the radiative scheme during the course of the simulation without scattering and absorption of the aerosols, in full-sky and clear-sky conditions. For the ERF of ozone, the linear ozone scheme of CNRM-CM6-1 allows simulations with ozone coefficients for a specific year, all other forcings remaining unchanged, and this offers a quite unique way to compute this ERF term. Such a methodology cannot be applied in a model with full chemistry like CNRM-ESM2-1.

Compared to reference data sets, MACv2 and MACv2-SP, and to MERRA-2, the PD CNRM-CM6-1 total AOD (0.10) is biased low, although in the range of aerosol models, with a too small transport away from source regions. Most of this bias comes from the anthropogenic aerosol AOD (0.018) over land. The CNRM-CM6-1 AAOD (4.510^{-3}) appears also weak, with the largest biases over biomass burning regions. The change in CDNC at cloud top from 1850 to 2014, used to characterize the Twomey effect, is larger (1.20) than that of MACv2-SP. However, in the end, total anthropogenic aerosol PD ERF and its two terms ERFari and ERFaci lie within the estimates of Zelinka et al. (2014) (-1.10 , -0.36 , and -0.81 W m^{-2} , respectively). These global means hide large spatial and seasonal differences.

Several piClim-aer-type simulations have been carried out both with CNRM-CM6-1 and CNRM-ESM2-1 to better understand their ERF values. In summary, these simulations reveal the small impact of the level of natural aerosols on the anthropogenic aerosol ERF but conversely the large change in computing the ERF from a simulation with monthly prescribed AODs and a simulation with interactive aerosols (ERFs of -0.74 and -0.97 W m^{-2} , respectively). Simulations to derive the ERF of an individual aerosol type indicate the predominant part of the sulfate ERF.

Over the historical period, CNRM-CM6-1 and CNRM-ESM2-1 have similar trends of anthropogenic aerosols, and these trends are lower than the MACv2 and MACv2-SP ones, possibly because of differences in emissions but also in overall aerosol representation (see Flato et al., 2013). Transient ERFs computed from a pair of AMIP-type simulations are confirmed when evaluated from pairs of 30 year fixed SSTs simulations. Zooming over Asia, the large negative trend that started in 1950 is very similar in both ERFaci and ERFari.

PD ozone mixing ratios of CNRM-CM6-1, CNRM-ESM2-1, and the CMIP6-OZ reference data set are within 10% throughout most of the stratosphere, with exceptions around the tropopause and in the mesosphere. The TCO is overall well simulated by the CNRM climate models, with compensating biases depending on the latitude though. Its historical evolution over 1960–2014 is, globally averaged, very close to that of the NIWA3.3 data set. Biases over this period reflect those of the PD, and latitude-dependent year-to-year variability of the model outputs is relatively realistic.

The PD CNRM-CM6-1 ozone ERF that represents a stratospheric ozone ERF, computed with a 70 year fixed SST simulation, is -0.040 ± 0.032 W m^{-2} , in coherence with literature. The transient ERFs, computed with two different methods, produce very similar results for the global mean total ERF: no trend over the whole period and opposite trends for the LW (positive trend) and SW (negative trend) ERF components.

Finally, interesting results in relation to ECS estimates include the satisfactory behavior of the CNRM-CM6-1 linear ozone scheme under 4xCO₂ conditions, while the ECS estimate of CNRM-CM6-1 with TACTIC_v2 differs noticeably from that of CNRM-CM6-1 with prescribed aerosols.

Results presented here give confidence that overall, the aerosol and ozone representations of both CNRM climate models are suitable for further studies by the scientific community that will analyze CMIP6 experiments. They also point out features that will require specific attention in future developments. In particular, attention will concern anthropogenic aerosols whose negative biases should be reduced by considering the nitrate and ammonium aerosols, as described in Drugé et al. (2019) who performed an evaluation of this extension of TACTIC over the Euro-Mediterranean region, and by introducing an absorbing part (brown carbon) in the organic aerosol. Adoption of recent developments, in particular concerning natural

aerosols over oceans, should also improve the realism of the aerosol representation. Finally, integration of a lower-troposphere chemistry, simple enough to be suitable for climate simulations, would benefit both to aerosol representation, allowing the parameterization of SOAs, and to lower tropospheric ozone.

Acronyms

AAOD	Aerosol Absorption Optical Depth
ACI	aerosol-cloud interaction
AerChemMIP	Aerosol Chemistry Model Intercomparison Project
AMIP	Atmosphere Model Intercomparison Project
AOD	Aerosol Optical Depth
ARI	aerosol-radiation interaction
AR5	Fifth Assessment Report of the IPCC
ASY	asymmetry parameter
BC	Black Carbon aerosol
CDNC	cloud droplet number concentration
CMIP6	Coupled Model Intercomparison Project 6
CNRM	Centre National Recherches Météorologiques
DD	dust aerosol
DMS	dimethylsulfide
ECs	Equilibrium Climate Sensitivity
ERF	Effective Radiative Forcing
ESM	Earth System Model
LW	longwave
MIP	Model Intercomparison Project
NIWA	National Institute of Water and Atmospheric Research
NRMSE	normalized root mean square error
OM	Organic Matter aerosol
PD	Present day
PI	preindustrial
RFMIP	Radiative Forcing MIP
SS	primary Sea-Salt aerosol
SSA	single scattering albedo
SST	sea surface temperature
SW	shortwave
TACTIC	Tropospheric Aerosols for Climate In CNRM-CM
TCO	total column ozone
TOA	top of the atmosphere

Acknowledgments

A number of components of the CNRM-CM6-1 and CNRM-ESM2-1 code are open source. The SURFEX code is available (Open-SURFEX) using a CECILL-C Licence (http://www.cecill.info/licences/Licence_CeCILL-C_V1-en.txt) at <http://www.umr-cnrm.fr/surfex>; NEMO-GELATO is also available at <https://opensource.umr-cnrm.fr/>; OASIS3-MCT can be downloaded at <https://verc.enes.org/oasis/download>; and XIOS can be downloaded at <https://forge.ipsl.jussieu.fr/ioserver>. For the ARPEGE-Climate v6 code and exact version applied to each component, in particular the aerosol and chemistry components, please contact the authors. CMIP6 CNRM-CM6-1 and CNRM-ESM2-1 experiments assessed in this paper are available on the Earth System Grid Federation (ESGF). Diagnostics from the other simulations shown are available upon request to the authors. We particularly acknowledge the support of the entire team in charge of the CNRM climate models and especially that of Antoinette Alias and Laurent Franchistegy for their technical assistance. Supercomputing time was provided by the Météo-France/DSI supercomputing center. We would like to thank Bodeker Scientific, funded by the New Zealand Deep South National Science Challenge, for providing the combined NIWA-BS total column ozone database. We thank Stefan Kinne for providing the MACv2 data and Stephanie Fiedler for providing the MACv2-SP data. The ESMValTool software has been used to produce figures in this paper (<http://doi.org/10.17874/ac8548f0315>, Version 1.1; Eyring et al., 2016). We acknowledge support from the European Unions Horizon 2020 Research and Innovation Programme under Grant Agreements 641816 (CRESCENDO) and 820829 (CONSTRAIN).

References

Andres, R. J., & Kasgnoc, A. D. (1998). A time-averaged inventory of subaerial volcanic sulfur emissions. *Journal of Geophysical Research*, 103, 25,251–25,261. <https://doi.org/10.1029/98JD02091>

Andrews, T., Gregory, J. M., & Webb, M. J. (2015). The dependence of radiative forcing and feedback on evolving patterns of surface temperature change in climate models. *Journal of Climate*, 28(4), 1630–1648. <https://doi.org/10.1175/JCLI-D-14-00545.1>

Bellouin, N., Rae, J., Jones, A., Johnson, C., Haywood, J., & Boucher, O. (2011). Aerosol forcing in the Climate Model Intercomparison Project (CMIP5) simulations by HadGEM2-ES and the role of ammonium nitrate. *Journal of Geophysical Research*, 116, D20206. <http://doi.org/10.1029/2011JD016074>

Boucher, O., & Lohmann, U. (1995). The sulfate-CCN-cloud albedo effect. *Tellus B*, 47(3), 281–300.

Boucher, O., Randall, D., Artaxo, P., Bretherton, C., Feingold, G., Forster, P., et al. (2013). Clouds and aerosols. In T. F. Stocker et al. (Eds.), *Climate Change 2013: The Physical Science Basis. Contribution of Working Group I to the Fifth Assessment Report of the Intergovernmental Panel on Climate Change*. Cambridge, United Kingdom and New York, NY, USA: Cambridge University Press

Bozzo, A., Benedetti, A., Flemming, J., Kipling, Z., & Rémy, S. (2019). An aerosol climatology for global models based on the tropospheric aerosol scheme in the Integrated Forecasting System of ECMWF. *Geoscientific Model Development Discussions*, 2019, 1–35. <http://doi.org/10.5194/gmd-2019-149>

Brasseur, G. P., Hauglustaine, D. A., Walters, S., Rasch, P. J., Müller, J.-F., Granier, C., & Tie, X. X. (1998). Mozart, a global chemical transport model for ozone and related chemical tracers: 1. Model description. *Journal of Geophysical Research*, 103(D21), 28,265–28,289. <http://doi.org/10.1029/98JD02397>

- Cappa, C. D., Onasch, T. B., Massoli, P., Worsnop, D. R., Bates, T. S., Cross, E. S., et al. (2012). Radiative absorption enhancements due to the mixing state of atmospheric black carbon. *Science*, *337*(6098), 1078–1081. <http://doi.org/10.1126/science.1223447>
- Carslaw, K., Lee, L., Reddington, C., Pringle, K., Rap, A., Forster, P., et al. (2013). Large contribution of natural aerosols to uncertainty in indirect forcing. *Nature*, *503*, 67–71. <http://doi.org/10.1038/nature12674>
- Checa-Garcia, R., Hegglin, M. I., Kinnison, D., Plummer, D. A., & Shine, K. P. (2018). Historical tropospheric and stratospheric ozone radiative forcing using the CMIP6 database. *Geophysical Research Letters*, *45*, 3264–3273. <http://doi.org/10.1002/2017GL076770>
- Cionni, I., Eyring, V., Lamarque, J. F., Randel, W. J., Stevenson, D. S., Wu, F., et al. (2011). Ozone database in support of CMIP5 simulations: Results and corresponding radiative forcing. *Atmospheric Chemistry and Physics*, *11*(21), 11,267–11,292. <http://doi.org/10.5194/acp-11-11267-2011>
- Collins, W. J., Lamarque, J., Schulz, M., Boucher, O., Eyring, V., Hegglin, M., et al. (2017). AerChemMIP: Quantifying the effects of chemistry and aerosols in CMIP6. *Geoscientific Model Development*, *10*(2), 585–607. <http://doi.org/10.5194/gmd-10-585-2017>
- Decharme, B., Delire, C., Minvielle, M., Colin, J., Vergnes, J.-P., Alias, A., et al. (2019). Recent changes in the ISBA-CTRIP land surface system for use in the CNRM-CM6 climate model and in global off-line hydrological applications. *Journal of Advances in Modeling Earth Systems*, *11*, 1207–1252. <http://doi.org/10.1029/2018MS001545>
- Dentener, F., Kinne, S., Bond, T., Boucher, O., Cofala, J., Generoso, S., et al. (2006). Emissions of primary aerosol and precursor gases in the years 2000 and 1750 prescribed data-sets for AeroCom. *Atmospheric Chemistry and Physics*, *6*(12), 4321–4344. <http://doi.org/10.5194/acp-6-4321-2006>
- Drugé, T., Nabat, P., Mallet, M., & Somot, S. (2019). Model simulation of ammonium and nitrate aerosols distribution in the Euro-Mediterranean region and their radiative and climatic effects over 1979–2016. *Atmospheric Chemistry and Physics*, *19*(6), 3707–3731. <http://doi.org/10.5194/acp-19-3707-2019>
- Eyring, V., Arblaster, J. M., Cionni, I., Sedek, J., Perlwitz, J., Young, P. J., et al. (2013). Long-term ozone changes and associated climate impacts in CMIP5 simulations. *Journal of Geophysical Research: Atmospheres*, *118*, 5029–5060. <http://doi.org/10.1002/jgrd.50316>
- Eyring, V., Bony, S., Meehl, G. A., Senior, C. A., Stevens, B., Stouffer, R. J., & Taylor, K. E. (2016). Overview of the Coupled Model Inter-comparison Project Phase 6 (CMIP6) experimental design and organization. *Geoscientific Model Development*, *9*(5), 1937–1958. <http://doi.org/10.5194/gmd-9-1937-2016>
- Eyring, V., Righi, M., Lauer, A., Evaldsson, M., Wenzel, S., Jones, C., et al. (2016). ESMValTool (v1.0)—A community diagnostic and performance metrics tool for routine evaluation of Earth system models in CMIP. *Geoscientific Model Development*, *9*(5), 1747–1802. <http://doi.org/10.5194/gmd-9-1747-2016>
- Fiedler, S., Stevens, B., Gidden, M., Smith, S. J., Riahi, K., & van Vuuren, D. (2019). First forcing estimates from the future CMIP6 scenarios of anthropogenic aerosol optical properties and an associated Twomey effect. *Geoscientific Model Development*, *12*(3), 989–1007. <http://doi.org/10.5194/gmd-12-989-2019>
- Fiedler, S., Stevens, B., & Mauritsen, T. (2017). On the sensitivity of anthropogenic aerosol forcing to model-internal variability and parameterizing a Twomey effect. *Journal of Advances in Modeling Earth Systems*, *9*, 1325–1341. <http://doi.org/10.1002/2017MS000932>
- Flato, G., Marotzke, J., Abiodun, B., Braconnot, P., Chou, S., Collins, W., et al. (2013). Evaluation of climate models. In T. Stocker et al. (Eds.), *Climate change 2013: The physical science basis. Contribution of Working Group I to the Fifth Assessment Report of the Intergovernmental Panel on Climate Change* (pp. 741–866). Cambridge, United Kingdom and New York, NY, USA: Cambridge University Press. <http://doi.org/10.1017/CBO9781107415324.020>
- Forster, P. M., Richardson, T., Maycock, A. C., Smith, C. J., Samset, B. H., Myhre, G., et al. (2016). Recommendations for diagnosing effective radiative forcing from climate models for CMIP6. *Journal of Geophysical Research: Atmospheres*, *121*, 12,460–12,475. <http://doi.org/10.1002/2016JD025320>
- Ghan, S. J. (2013). Technical note: Estimating aerosol effects on cloud radiative forcing. *Atmospheric Chemistry and Physics*, *13*(19), 9971–9974. <http://doi.org/10.5194/acp-13-9971-2013>
- Gregory, J. M., Ingram, W. J., Palmer, M. A., Jones, G. S., Stott, P. A., Thorpe, R. B., et al. (2004). A new method for diagnosing radiative forcing and climate sensitivity. *Geophysical Research Letters*, *31*, L03205. <http://doi.org/10.1029/2003GL018747>
- Grythe, H., Ström, J., Krejci, R., Quinn, P., & Stohl, A. (2014). A review of sea-spray aerosol source functions using a large global set of sea salt aerosol concentration measurements. *Atmospheric Chemistry and Physics*, *14*(3), 1277–1297. <http://doi.org/10.5194/acp-14-1277-2014>
- Hoesly, R. M., Smith, S. J., Feng, L., Klimont, Z., Janssens-Maenhout, G., Pitkanen, T., et al. (2018). Historical (1750–2014) anthropogenic emissions of reactive gases and aerosols from the Community Emissions Data System (CEDS). *Geoscientific Model Development*, *11*(1), 369–408. <http://doi.org/10.5194/gmd-11-369-2018>
- Holben, B. N., Eck, T. F., Slutsker, I., Tanré, D., Buis, J. P., Setzer, A., et al. (1998). AERONET—A federated instrument network and data archive for aerosol characterization. *Remote Sensing of Environment*, *66*, 1–16. [http://doi.org/10.1016/S0034-4257\(98\)00031-5](http://doi.org/10.1016/S0034-4257(98)00031-5)
- Hossaini, R., Chipperfield, M. P., Montzka, S. A., Rap, A., Dhomse, S., & Feng, W. (2015). Efficiency of short-lived halogens at influencing climate through depletion of stratospheric ozone.
- Huneeus, N., Chevallier, F., & Boucher, O. (2012). Estimating aerosol emissions by assimilating observed aerosol optical depth in a global aerosol model. *Atmospheric Chemistry and Physics*, *12*(10), 4585–4606. <http://doi.org/10.5194/acp-12-4585-2012>
- Iglesias-Suarez, F., Kinnison, D. E., Rap, A., Maycock, A. C., Wild, O., & Young, P. J. (2018). Key drivers of ozone change and its radiative forcing over the 21st century. *Atmospheric Chemistry and Physics*, *18*(9), 6121–6139. <http://doi.org/10.5194/acp-18-6121-2018>
- Inness, A., Ades, M., Agustí-Panareda, A., Barré, J., Benedictow, A., Blechschmidt, A.-M., et al. (2019). The CAMS reanalysis of atmospheric composition. *Atmospheric Chemistry and Physics*, *19*(6), 3515–3556.
- Jaeglé, L., Quinn, P. K., Bates, T. S., Alexander, B., & Lin, J.-T. (2011). Global distribution of sea salt aerosols: New constraints from in situ and remote sensing observations. *Atmospheric Chemistry and Physics*, *11*(7), 3137–3157. <http://doi.org/10.5194/acp-11-3137-2011>
- Johnson, B. T., Haywood, J. M., Langridge, J. M., Darbyshire, E., Morgan, W. T., Szpek, K., et al. (2016). Evaluation of biomass burning aerosols in the HadGEM3 climate model with observations from the SAMBBA field campaign. *Atmospheric Chemistry and Physics*, *16*(22), 14,657–14,685. <http://doi.org/10.5194/acp-16-14657-2016>
- Kettle, A. J., Andreae, M. O., Amouroux, D., Andreae, T. W., Bates, T. S., Berresheim, H., et al. (1999). A global database of sea surface dimethylsulfide (DMS) measurements and a procedure to predict sea surface DMS as a function of latitude, longitude, and month. *Global Biogeochemical Cycles*, *13*(2), 399–444. <http://doi.org/10.1029/1999GB900004>
- Kinne, S. (2019). The MACv2 aerosol climatology. *Tellus B Chemical and Physical Meteorology*, *71*, 1–21. <http://doi.org/10.1080/16000889.2019.1623639>
- Kinne, S., O'Donnell, D., Stier, P., Kloster, S., Zhang, K., Schmidt, H., et al. (2013). Mac-v1: A new global aerosol climatology for climate studies. *Journal of Advances in Modeling Earth Systems*, *5*, 704–740. <http://doi.org/10.1002/jame.20035>

- Kinne, S., Schulz, M., Textor, C., Guibert, S., Balkanski, Y., Bauer, S. E., et al. (2006). An AeroCom initial assessment optical properties in aerosol component modules of global models. *Atmospheric Chemistry and Physics*, 6(7), 1815–1834. <http://doi.org/10.5194/acp-6-1815-2006>
- Koffi, B., Schulz, M., Breon, F.-Marie, Dentener, F., Steensen, B. M., Griesfeller, J., et al. (2016). Evaluation of the aerosol vertical distribution in global aerosol models through comparison against CALIOP measurements: AeroCom phase II results. *Journal of Geophysical Research: Atmospheres*, 121, 7254–7283. <http://doi.org/10.1002/2015JD024639>
- Kok, J. F. (2011). A scaling theory for the size distribution of emitted dust aerosols suggests climate models underestimate the size of the global dust cycle. *Proceedings of the National Academy of Sciences*, 108(3), 1016–1021. <http://doi.org/10.1073/pnas.1014798108>
- Krekov, G. (1993). Models of atmospheric aerosols, in aerosol effects on climate edited by: Jennings, S. G.
- Lacagnina, C., Hasekamp, O. P., Bian, H., Curci, G., Myhre, G., Noije, T., et al. (2015). Aerosol single-scattering albedo over the global oceans: Comparing PARASOL retrievals with AERONET, OMI, and AeroCom models estimates. *Journal of Geophysical Research: Atmospheres*, 120, 9814–9836. <http://doi.org/10.1002/2015JD023501>
- Marticorena, B., & Bergametti, G. (1995). Modeling the atmospheric dust cycle: 1. Design of a soil-derived dust emission scheme. *Journal of Geophysical Research: Atmospheres*, 100(D8), 16,415–16,430. <http://doi.org/10.1029/95JD00690>
- Matthes, K., Funke, B., Andersson, M. E., Barnard, L., Beer, J., Charbonneau, P., et al. (2017). Solar forcing for CMIP6 (v3.2). *Geoscientific Model Development*, 10(6), 2247–2302. <http://doi.org/10.5194/gmd-10-2247-2017>
- Maycock, A. C., Matthes, K., Tegtmeier, S., Schmidt, H., Thiéblemont, R., Hood, L., et al. (2018). The representation of solar cycle signals in stratospheric ozone—Part 2: Analysis of global models. *Atmospheric Chemistry and Physics*, 18(15), 11,323–11,343. <http://doi.org/10.5194/acp-18-11323-2018>
- Maycock, A. C., Randel, W. J., Steiner, A. K., Karpechko, A. Y., Christy, J., Saunders, R., et al. (2018). Revisiting the mystery of recent stratospheric temperature trends. *Geophysical Research Letters*, 45, 9919–9933. <http://doi.org/10.1029/2018GL078035>
- McCoy, D. T., Bender, F. A.-M., Mohrmann, J. K. C., Hartmann, D. L., Wood, R., & Grosvenor, D. P. (2017). The global aerosol-cloud first indirect effect estimated using MODIS, MERRA, and AeroCom. *Journal of Geophysical Research: Atmospheres*, 122, 1779–1796. <http://doi.org/10.1002/2016JD026141>
- Meinshausen, M., Meinshausen, M., Vogel, E., Nauels, A., Lorbacher, K., Meinshausen, N., et al. (2017). Historical greenhouse gas concentrations for climate modelling (CMIP6). *Geoscientific Model Development*, 10(5), 2057–2116. <http://doi.org/10.5194/gmd-10-2057-2017>
- Menon, S., Genio, A. D. D., Koch, D., & Tselioudis, G. (2002). GCM, simulations of the aerosol indirect effect: Sensitivity to cloud parameterization and aerosol burden. *Journal of the Atmospheric Sciences*, 59(3), 692–713.
- Michou, M., Nabat, P., & Saint-Martin, D. (2015). Development and basic evaluation of a prognostic aerosol scheme (v1) in the CNRM climate model CNRM-CM6. *Geoscientific Model Development*, 8(3), 501–531. <http://doi.org/10.5194/gmd-8-501-2015>
- Michou, M., Saint-Martin, D., Teyssède, H., Alias, A., Karcher, F., Olivieri, D., et al. (2011). A new version of the CNRM chemistry-climate model, CNRM-CCM: Description and improvements from the CCMVAL-2 simulations. *Geoscientific Model Development*, 4(4), 873–900. <http://doi.org/10.5194/gmd-4-873-2011>
- Monge-Sanz, B. M., Chipperfield, M. P., Cariolle, D., & Feng, W. (2011). Results from a new linear O₃ scheme with embedded heterogeneous chemistry compared with the parent full-chemistry 3-D CTM. *Atmospheric Chemistry and Physics*, 11(3), 1227–1242. <http://doi.org/10.5194/acp-11-1227-2011>
- Morcrette, J.-J., Benedetti, A., & Ghelli, A. (2011). K. J., and Tompkins A.P. *Aerosol-cloud-radiation interactions and their impact on ECMWF/MACC forecasts*, (660), 36. <http://doi.org/10.21957/wjuxaujrn>
- Morgenstern, O., Hegglin, M. I., Rozanov, E., O'Connor, F. M., Abraham, N. L., Akiyoshi, H., et al. (2017). Review of the global models used within phase 1 of the Chemistry–Climate Model Initiative (CCMI). *Geoscientific Model Development*, 10(2), 639–671. <http://doi.org/10.5194/gmd-10-639-2017>
- Myhre, G., Aas, W., Cherian, R., Collins, W., Faluvegi, G., Flanner, M., et al. (2017). Multi-model simulations of aerosol and ozone radiative forcing due to anthropogenic emission changes during the period 1990–2015. *Atmospheric Chemistry and Physics*, 17(4), 2709–2720. <http://doi.org/10.5194/acp-17-2709-2017>
- Myhre, G., Samset, B. H., Schulz, M., Balkanski, Y., Bauer, S., Bernsten, T. K., et al. (2013). Radiative forcing of the direct aerosol effect from AeroCom phase ii simulations. *Atmospheric Chemistry and Physics*, 13(4), 1853–1877. <http://doi.org/10.5194/acp-13-1853-2013>
- Myhre, G., Shindell, D., Bréon, F. M., Collins, W., Fuglestedt, J., Huang, J., et al. (2013). Anthropogenic and natural radiative forcing. In T. F. Stocker et al. (Eds.), *Climate Change 2013: The Physical Science Basis. Contribution of Working Group I to the Fifth Assessment Report of the Intergovernmental Panel on Climate Change* (pp. 659–740). Cambridge, UK: Cambridge University Press. <http://doi.org/10.1017/CBO9781107415324.018>
- Nabat, P., Somot, S., Mallet, M., Chiapello, I., Morcrette, J. J., Solmon, F., et al. (2013). A 4-D climatology (1979–2009) of the monthly tropospheric aerosol optical depth distribution over the Mediterranean region from a comparative evaluation and blending of remote sensing and model products. *Atmospheric Measurement Techniques*, 6, 1287–1314. <http://doi.org/10.5194/amt-6-1287-2013>
- Nabat, P., Somot, S., Mallet, M., Michou, M., Sevault, F., Friouech, F., et al. (2015). Dust aerosol radiative effects during summer 2012 simulated with a coupled regional aerosol–atmosphere–ocean model over the Mediterranean. *Atmospheric Chemistry and Physics*, 15(6), 3303–3326. <http://doi.org/10.5194/acp-15-3303-2015>
- Ng, N. L., Canagaratna, M. R., Zhang, Q., Jimenez, J. L., Tian, J., Ulbrich, I. M., et al. (2010). Organic aerosol components observed in northern hemispheric datasets from aerosol mass spectrometry. *Atmospheric Chemistry and Physics*, 10(10), 4625–4641. <http://doi.org/10.5194/acp-10-4625-2010>
- Nordling, K., Korhonen, H., Räisänen, P., Alper, M. E., Uotila, P., O'Donnell, D., & Merikanto, J. (2019). Role of climate model dynamics in estimated climate responses to anthropogenic aerosols. *Atmospheric Chemistry and Physics Discussions*, 2019, 1–22. <http://doi.org/10.5194/acp-2018-1335>
- Nowack, P. J., Abraham, N. Luke, Braesicke, P., & Pyle, J. A. (2018). The impact of stratospheric ozone feedbacks on climate sensitivity estimates. *Journal of Geophysical Research: Atmospheres*, 123, 4630–4641. <http://doi.org/10.1002/2017JD027943>
- Nowack, J. P., Luke Abraham, N., Maycock, A., Braesicke, P., Gregory, J., Joshi, M., et al. (2015). A large ozone-circulation feedback and its implications for global warming assessments. *Nature climate change*, 5, 41–45. <http://doi.org/10.1038/nclimate2451>
- Pan, X., Chin, M., Gautam, R., Bian, H., Kim, D., Colarco, P. R., et al. (2015). A multi-model evaluation of aerosols over South Asia: Common problems and possible causes. *Atmospheric Chemistry and Physics*, 15(10), 5903–5928. <http://doi.org/10.5194/acp-15-5903-2015>
- Pincus, R., Forster, P. M., & Stevens, B. (2016). The radiative forcing model intercomparison project (RFMIP): Experimental protocol for CMIP6. *Geoscientific Model Development*, 9(9), 3447–3460. <http://doi.org/10.5194/gmd-9-3447-2016>
- Quaas, J., & Boucher, O. (2005). Constraining the first aerosol indirect radiative forcing in the LMDZ GCM using POLDER and MODIS satellite data. *Geophysical Research Letters*, 32, L17814. <http://doi.org/10.1029/2005GL023850>

- Quaas, J., Boucher, O., & Lohmann, U. (2006). Constraining the total aerosol indirect effect in the LMDZ and ECHAM4 GCMs using MODIS satellite data. *Atmospheric Chemistry and Physics*, 6(4), 947–955. <http://doi.org/10.5194/acp-6-947-2006>
- Quaas, J., Ming, Y., Menon, S., Takemura, T., Wang, M., Penner, J. E., et al. (2009). Aerosol indirect effects general circulation model intercomparison and evaluation with satellite data. *Atmospheric Chemistry and Physics*, 9(22), 8697–8717. <http://doi.org/10.5194/acp-9-8697-2009>
- Randles, C. A., da Silva, A. M., Buchard, V., Colarco, P. R., Darmenov, A., Govindaraju, R., et al. (2017). The MERRA-2 aerosol reanalysis, 1980 onward. Part I: System description and data assimilation evaluation. *Journal of Climate*, 30(17), 6823–6850. <http://doi.org/10.1175/JCLI-D-16-0609.1>
- Ringer, M. A., Andrews, T., & Webb, M. J. (2014). Global-mean radiative feedbacks and forcing in atmosphere-only and coupled atmosphere-ocean climate change experiments. *Geophysical Research Letters*, 41, 4035–4042. <http://doi.org/10.1002/2014GL060347>
- Sander, S. P., Abbatt, J., Barker, J. R., Burkholder, J. B., Friedl, R. R., Golden, D. M., et al. (2011). Chemical kinetics and photochemical data for use in atmospheric studies, evaluation no. 17. *JPL Publication*, 5, 10–6.
- Séférian, R., Nabat, P., Michou, M., Saint-Martin, D., Voldoire, A., Colin, J., et al. (2019). Evaluation of CNRM Earth-system model, CNRM-ESM 2-1: Role of Earth system processes in present-day and future climate, 11. <http://doi.org/10.1029/2019MS001791>
- Shindell, D. T., Lamarque, J.-F., Schulz, M., Flanner, M., Jiao, C., Chin, M., et al. (2013). Radiative forcing in the ACCMIP historical and future climate simulations. *Atmospheric Chemistry and Physics*, 13(6), 2939–2974. <http://doi.org/10.5194/acp-13-2939-2013>
- Shindell, D. T., Pechony, O., Voulgarakis, A., Faluvegi, G., Nazarenko, L., Lamarque, J.-F., et al. (2013). Interactive ozone and methane chemistry in GISS-E2 historical and future climate simulations. *Atmospheric Chemistry and Physics*, 13(5), 2653–2689. <http://doi.org/10.5194/acp-13-2653-2013>
- Smirnov, A., Holben, B. N., Slutsker, I., Giles, D. M., McClain, C. R., Eck, T. F., et al. (2009). Maritime aerosol network as a component of aerosol robotic network. *Journal of Geophysical Research: Atmospheres*, 114, D06204. <http://doi.org/10.1029/2008JD011257>
- Sockol, A., & Small Griswold, J. D. (2017). Intercomparison between CMIP5 model and MODIS satellite-retrieved data of aerosol optical depth, cloud fraction, and cloud-aerosol interactions: CMIP5 and MODIS AOD-CF interactions. *Earth and Space Science*, 4, 485–505. <http://doi.org/10.1002/2017EA000288>
- Stevens, B., Fiedler, S., Kinne, S., Peters, K., Rast, S., Müsse, J., et al. (2017). MACv2-SP: A parameterization of anthropogenic aerosol optical properties and an associated Twomey effect for use in CMIP6. *Geoscientific Model Development*, 10(1), 433–452. <http://doi.org/10.5194/gmd-10-433-2017>
- Struthers, H., Bodeker, G. E., Austin, J., Bekki, S., Cionni, I., Dameris, M., et al. (2009). The simulation of the Antarctic ozone hole by chemistry-climate models. *Atmospheric Chemistry and Physics*, 9(17), 6363–6376. <http://doi.org/10.5194/acp-9-6363-2009>
- Szopa, S., Balkanski, Y., Schulz, M., Bekki, S., Cugnet, D., Fortems-Cheiney, A., et al. (2013). Aerosol and ozone changes as forcing for climate evolution between 1850 and 2100. *Climate Dynamics*, 40(9), 2223–2250. <http://doi.org/10.1007/s00382-012-1408-y>
- Textor, C., Schulz, M., Guibert, S., Kinne, S., Balkanski, Y., Bauer, S., et al. (2006). Analysis and quantification of the diversities of aerosol life cycles within AeroCom. *Atmospheric Chemistry and Physics*, 6(7), 1777–1813. <http://doi.org/10.5194/acp-6-1777-2006>
- Thomason, L. W., Ernest, N., Millán, L., Rieger, L., Bourassa, A., Vernier, J.-P., et al. (2018). A global space-based stratospheric aerosol climatology: 1979–2016. *Earth System Science Data*, 10(1), 469–492. <http://doi.org/10.5194/essd-10-469-2018>
- Tiitta, P., Vakkari, V., Croteau, P., Beukes, J. P., van Zyl, P. G., Josipovic, M., et al. (2014). Chemical composition, main sources and temporal variability of PM₁ aerosols in southern African grassland. *Atmospheric Chemistry and Physics*, 14(4), 1909–1927. <http://doi.org/10.5194/acp-14-1909-2014>
- Toll, V., Gleeson, E., Nielsen, K., Mnnik, A., Masek, J., Rontu, L., & Post, P. (2016). Impacts of the direct radiative effect of aerosols in numerical weather prediction over Europe using the ALADIN-HIRLAM NWP system. *Atmospheric Research*, 172, 1016. <http://doi.org/10.1016/j.atmosres.2016.01.003>
- Tsigaridis, K., Daskalakis, N., Kanakidou, M., Adams, P. J., Artaxo, P., Bahadur, R., et al. (2014). The AeroCom evaluation and intercomparison of organic aerosol in global models. *Atmospheric Chemistry and Physics*, 14(19), 10,845–10,895. <http://doi.org/10.5194/acp-14-10845-2014>
- Turpin, J. B., & Lim, H.-J. (2001). Species contributions to PM_{2.5} mass concentrations: Revisiting common assumptions for estimating organic mass. *Aerosol Science and Technology - AEROSOL SCI TECH*, 35, 602–610. <http://doi.org/10.1080/02786820120515454>
- van Marle, M. J. E., Kloster, S., Magi, B. I., Marlon, J. R., Daniua, A.-L., Field, R. D., et al. (2017). Historic global biomass burning emissions for CMIP6 (BB4CMIP) based on merging satellite observations with proxies and fire models (1750–2015). *Geoscientific Model Development*, 10(9), 3329–3357. <http://doi.org/10.5194/gmd-10-3329-2017>
- Voldoire, A., Saint-Martin, D., Sénési, S., Decharme, B., Alias, A., Chevallier, M., et al. (2019). Evaluation of CMIP6 deck experiments with CNRM-CM6-1. *Journal of Advances in Modeling Earth Systems*, 11, 2177–2213. <http://doi.org/10.1029/2019MS001683>
- Voldoire, A., Sanchez-Gomez, E., y Méliá, D. Salas, Decharme, B., Cassou, C., Sénési, S., et al. (2013). The CNRM-CM5.1 global climate model: Description and basic evaluation. *Climate Dynamics*, 40(9-10), 2091–2121. <http://doi.org/10.1007/s00382-011-1259-y>
- Wales, Pamela A., Salawitch, Ross J., Nicely, Julie M., Anderson, Daniel C., Canty, Timothy P., Baidar, S., et al. (2018). Stratospheric injection of brominated very short-lived substances: Aircraft observations in the western Pacific and representation in global models. *Journal of Geophysical Research: Oceans*, 123, 5690–5719. <http://doi.org/10.1029/2017JD027978>
- Watson, L., Michou, M., Nabat, P., & Saint-Martin, D. (2018). Assessment of CNRM coupled ocean-atmosphere model sensitivity to the representation of aerosols. *Climate Dynamics*, 51(7), 2877–2895. <http://doi.org/10.1007/s00382-017-4054-6>
- WMO scientific assessment of ozone depletion: 2018 (2018). Global Ozone Research and Monitoring Project-Report No. 58.
- Zelinka, M. D., Andrews, T., Forster, P. M., & Taylor, K. E. (2014). Quantifying components of aerosol-cloud-radiation interactions in climate models. *Journal of Geophysical Research: Atmospheres*, 119, 7599–7615. <https://doi.org/10.1002/2014JD021710>
- Zeng, S., Riedi, J., Treppe, C. R., Winker, D. M., & Hu, Y.-X. (2014). Study of global cloud droplet number concentration with A-Train satellites. *Atmospheric Chemistry and Physics*, 14(14), 7125–7134. <http://doi.org/10.5194/acp-14-7125-2014>
- Zhang, J., Tian, W., Xie, F., Chipperfield, M. P., Feng, W., Son, S.-W., et al. (2018). Stratospheric ozone loss over the Eurasian continent induced by the polar vortex shift. *Nature Communications*, 9(1), 206. <http://doi.org/10.1038/s41467-017-02565-2>
- Zhang, A., Wang, Y., Zhang, Y., Weber, R. J., Song, Y., Ke, Z., & Zou, Y. (2019). Modeling global radiative effect of brown carbon: A larger heating source in the tropical free troposphere than black carbon. *Atmospheric Chemistry and Physics Discussions*, 2019, 1–36. <http://doi.org/10.5194/acp-2019-594>
- Zuidema, P., Sedlacek III, A. J., Flynn, C., Springston, S., Delgadillo, R., Zhang, J., et al. (2018). The ascension island boundary layer in the remote Southeast Atlantic is often smoky. *Geophysical Research Letters*, 45, 4456–4465. <http://doi.org/10.1002/2017GL076926>